

1 Impact of boundary layer stability on urban park  
2 cooling effect intensity

3

4 *Authors: Martial Haeffelin<sup>1</sup>, Jean-François Ribaud<sup>2</sup>, Jonnathan Céspedes<sup>2</sup>, Jean-*  
5 *Charles Dupont<sup>3</sup>, Aude Lemonsu<sup>4</sup>, Valéry Masson<sup>4</sup>, Tim Nagel<sup>4</sup>, Simone Kotthaus<sup>2</sup>*

6

7 <sup>1</sup> *Institut Pierre Simon Laplace (IPSL), CNRS, Ecole polytechnique, Institut Polytechnique de Paris, 91128*  
8 *Palaiseau Cedex, France*

9 <sup>2</sup> *Laboratoire de Météorologie Dynamique (LMD-IPSL), Ecole polytechnique, Institut Polytechnique de*  
10 *Paris, 91128 Palaiseau Cedex, France*

11 <sup>3</sup> *Institut Pierre Simon Laplace (IPSL), Université Versailles Saint-Quentin-en-Yvelines, 78240*  
12 *Guyancourt, France*

13 <sup>4</sup> *Centre national de recherches météorologiques (CNRM), Université de Toulouse, Météo-France,*  
14 *CNRS, Toulouse, France*

15

16 Correspondence to: Martial Haeffelin (martial.haeffelin@ipsl.fr)

## 17 Abstract

18 The added heat in cities amplifies the health risks of heat waves. At night under calm winds  
19 and cloud free skies, the air in the urban canopy layer can be several degrees warmer than in  
20 rural areas. This lower nocturnal cooling in the built-up settings poses severe health risks to  
21 the urban inhabitants as indoor spaces cannot be ventilated effectively. With heat waves  
22 becoming more frequent and more intense in future climates, many cities are expanding their  
23 green spaces with the aim to introduce cooling through shading, evaporation, and lower heat  
24 storage capacities. In this study, it is assessed how the evening and night-time cooling effect  
25 of urban parks (relative to nearby built-up settings) varies with the park size and the meso-  
26 scale atmospheric conditions during warm summer periods. Using a combination of  
27 meteorological surface station data and compact radiosondes, the cooling effect is quantified  
28 for several urban parks (about 15 ha) and urban woods (about 900 ha). A profiling Doppler  
29 wind lidar deployed in the city centre is used to measure turbulent vertical mixing conditions  
30 in the urban boundary layer. We find that the maximum nocturnal cooling effects in urban  
31 parks range around 1-5°C during a one-week heat wave event in mid-July 2022 but also in  
32 general during summer 2022 (June-August). Three atmospheric stability and mixing regimes  
33 are identified that explain the night-to-night variability in park cooling effect. We find that  
34 very low turbulent vertical mixing in the urban boundary layer ( $< 0.05 \text{ m}^2\text{s}^{-2}$ ) results in the  
35 strongest evening cooling in both rural settings and urban parks and the weakest cooling in  
36 the built-up environment. This regime specifically occurs during heat waves in connection  
37 with large-scale advection of hot air over the region and corresponding subsidence. When  
38 nocturnal turbulent vertical mixing above the city is stronger, the evening cooling in urban  
39 green spaces is less efficient so that the atmospheric stratification above both urban parks  
40 and woods is less stable and temperature contrasts compared to the built-up environment  
41 are less pronounced. These results highlight that urban green spaces have a significant cooling  
42 potential during heat waves, with maximum effects at night as advection and mixing transport  
43 processes are minimal. This suggests adapting the opening hours of public parks to enable  
44 residents to benefit from these cooling islands.

45

Supprimé: -

## 47 1 - Introduction

48 Excess heat in cities has impacts on human comfort, labour productivity, and health. Mortality  
49 has been linked to exceptionally high temperatures during summertime heat waves both at  
50 night and during the day (Basu et al. 2002; Keatinge et al. 2000; Pirard et al. 2005). During the  
51 day, it is the outdoor radiative temperature that poses the most significant health risk. At  
52 night, indoor temperatures are particularly important as people need to rest and indoor air  
53 must be vented to cool the building for the upcoming day. However, urban inhabitants can  
54 be particularly exposed to excessive and prolonged heat stress at night as the city and the  
55 buildings do not cool efficiently, preventing necessary nocturnal rest. Hot nights following hot  
56 days have been shown to make an important contribution to heat-related mortality (Murage  
57 et al. 2017; Royé et al., 2021).

58

59 Reducing people's exposure to heat in cities can be addressed through urban planning  
60 strategies. Increasing the vegetation fraction of urban areas is a widely accepted strategy to  
61 mitigate urban heat risk by effectively reducing heat storage uptake during daytime  
62 (Grimmond and Oke, 2002). Trees can provide efficient shading, reducing daytime air  
63 temperatures by several degrees below their canopy, while evapotranspirative cooling  
64 provided by vegetation, including trees, shrubs and grass, maintain the green space  
65 temperature several degrees below that of the built-up environment (Shashua-Bar and  
66 Hoffman, 2000). Green infrastructures also show cooling effects at night, through continued  
67 evapotranspiration after sunset, generally larger sky-view factors in urban parks than in built-  
68 up environments, and lower heat capacities. However, reduced radiative cooling and  
69 ventilation can retain heat below the canopy at night (Taha et al. 1991).

70

71 The cooling effect intensity of urban green infrastructure has been shown to be highly variable  
72 (Bowler et al. 2010; Shoulika et al 2014). Doick et al (2014) point to a lack of certainty on the  
73 variables that drive the park cooling effects and on the multiple roles of trees and  
74 greenspaces. Spatial contrasts in nocturnal temperatures between green infrastructure and  
75 nearby built-up areas depend on park perimeter and area (Gao et al. 2022; Cai et al. 2023),  
76 on proportion of grass and trees, on tree size (Zhu et al. 2021), on vegetation types and  
77 arrangements (street trees vs parks), on density of vegetation (Holmer et al 2013), on park

Supprimé: whereby

Supprimé: The g

80 topography (Barradas 1991; Chang et al. 2007), and on local climates (Ibsen et al. 2021). Other  
81 authors investigated the spatial extent of cooling by urban parks, i.e. the *cooling effect*  
82 *distance*, showing that it depends on both park size and park greenness (e.g. Zhu et al 2021).  
83 From a recent review of park cooling effect studies conducted by Aram et al. (2019), we  
84 conclude that most studies focus on the impact of park characteristics and investigations on  
85 the impact of meteorological conditions on park cooling effects are rare.

86  
87 The impact of meteorological conditions, such as cloudiness, wind and turbulence on  
88 differential cooling is studied mostly at regional scale in terms of their impact on the urban  
89 heat island (UHI) intensity (Oke 2017). While the influence of cloud cover and wind is rather  
90 established (e.g. Morris et al. 2001, Lin et al. 2022), also the occurrence and characteristics of  
91 night-time low-level jets are found to influence UHI intensity (Lemonsu et al. 2009; Cespedes  
92 et al. 2024). However, the impact of local- to meso-scale meteorological phenomena on  
93 cooling effects of urban green infrastructure is not well quantified.

94  
95 The combined effects of green infrastructure characteristics and meteorological regimes on  
96 nocturnal cooling must hence be better understood so that the cooling effect of urban  
97 renaturation projects can be quantified more precisely. Which conditions affect the park  
98 cooling effect intensity? What is the relative impact of park characteristics and meteorological  
99 processes in the urban boundary layer on the cooling intensity ?

100  
101 The overall objective of this study is to quantify in detail the nocturnal cooling effects of urban  
102 parks during warm summertime conditions, taking into account potential cooling effects from  
103 the rural surroundings. We carried out this study in the framework of the Heat and Health in  
104 Cities project (H2C, Lemonsu et al. 2024) that focuses on the effects of excessive summertime  
105 heat and air pollution on human vulnerability (Forceville et al. 2024) with the Paris region  
106 (France) as a study area. A dedicated field campaign was designed and carried out in the city  
107 of Paris and the surrounding region to monitor spatial and temporal variations in key  
108 atmospheric thermodynamic variables in the urban canopy layer and urban boundary layer  
109 during summer 2022. The measurements performed, including near-surface and vertical  
110 profiles of temperature, humidity, wind and turbulence, and data analysis methodology are  
111 presented in Section 2. Section 3 presents the analysis of urban park cooling effects in relation

112 to regional UHI and their variability during summer 2022, with a focus on a one-week heat  
113 wave event. Next (Section 4), we investigate the characteristics of the urban boundary layer  
114 structure under three distinct atmospheric turbulence regimes and their influence on park  
115 cooling effects. Finally, we quantify the role of atmospheric stability and vertical turbulent  
116 mixing on differential evening cooling between built-up locations, urban parks and rural  
117 settings (Section 5).

118

## 119 2 - Data and methodologies

120 The present study is based upon data collected in the Paris region during the first Special  
121 Observation Period of the Heat and Health in Cities project (SOP 2022, Figure 1), which was  
122 conducted during summer 2022 (Lemonsu et al., 2024ab). This campaign also benefited from  
123 measurements carried out in the context of other research initiatives such as the Paris 2024  
124 Olympics WMO Research and Development Project (RDP-2024) and the ACTRIS research  
125 infrastructure (Laj et al. 2024). This multi-project context motivated the pooling of resources,  
126 a coordinated strategy for the organisation of the summer-2022 experimental campaigns, and  
127 the development of a joint data repository under the name PANAME (PARis region urbaN  
128 Atmospheric observations and models for Multidisciplinary rEsearch - see  
129 <https://paname.aeris-data.fr/>).

130

### 131 2.1 Datasets used in the study

132 This study combines continuous measurements collected from June to August 2022 and 14  
133 one-day intensive observation periods (IOPs), with data collected from mid-June to the end  
134 of July 2022. Measurement locations are shown in Figure 1.

135

#### 136 i) Surface meteorological stations

137 Météo France's operational network consists of some fifty ground-based weather stations in  
138 the Paris region measuring at least air temperature at 2 m AGL with a 6-minute acquisition  
139 time step. A few stations provide additional meteorological parameters such as wind speed  
140 and direction at 10 m AGL, global incoming radiation, precipitation, and cloud cover. The

141 stations are spread across the region in different areas, but are always installed on the ground  
142 on an open lawn (according to WMO recommendations).

143

144 We selected six stations to represent rural settings (Local Climate Zone, Stewart and Oke  
145 2012) of the Paris region (Figure 1), located in Changis, Courdimanche, Fresnoy-La-Riviere,  
146 Maule, Melun, and Pontoise, which is similar to the stations selected by Lemonsu et al. (2015).

147 The stations are geographically distributed in all directions relative to the city centre of Paris  
148 and located at altitudes ranging 50-90 m above sea level (ASL). In our study, the reference  
149 rural setting conditions of temperature, wind speed and direction are computed as the  
150 average of the variables measured at those six stations (Changis, Courdimanche, Melun, and  
151 Pontoise stations).

152

153 Near-surface urban park weather conditions are documented by a Météo-France weather  
154 station located in the Montsouris Park, a 15-ha park located in the 14<sup>th</sup> district, south of the  
155 Paris city centre. The station, located at an elevation of 75 m ASL, provides 2-m air  
156 temperature and humidity measurements. Wind speed and direction are measured at 25 m  
157 above ground level (AGL). A detailed description of temperature measurements in the  
158 Montsouris Park is provided by Dahech et al. (2020).

159

160 The Paris built-up setting conditions are sampled using Internet of Things (IoT) temperature  
161 and humidity measurements. This compact technology opens up new perspectives in  
162 meteorological measurements, particularly in urban environments where measurement and  
163 installation conditions are sometimes complicated. More than twenty IoT stations (DecentLab  
164 DL-SHT35-001 - air temperature and humidity sensor with radiation shield for LoRaWAN) have  
165 been installed in central Paris starting in July 2022. These are compact and lightweight  
166 stations installed on lampposts at a height of approximately 5 m AGL, following the  
167 recommendations made by Oke (2006). The stations have been installed on the north side of  
168 the lampposts to limit sensor warming through solar irradiance. The reference built-up setting  
169 temperature is computed as the average temperature recorded by four IoT stations located  
170 within 500 m of each other, in the highly urbanised neighbourhood of the Paris Opera House  
171 (hereafter referred to as Opera). Note that these stations were operational only from July 8,  
172 2022. For the period prior to this date (1 June to 7 July), the built-up setting temperature is

173 derived from the Météo France weather station Lariboisière Hospital (10<sup>th</sup> district of Paris)  
174 which is located 2 km northeast of the Opera neighbourhood in an equally dense built-up  
175 setting. Comparisons of temperatures measured at Lariboisière and Opera during July and  
176 August 2022 do not reveal any significant differences (not shown). The built-up setting  
177 temperature (at Lariboisière and Opera) is considered not influenced by green space cooling,  
178 as the closest urban park is about 1 km away and cooling effect distances of parks reported  
179 in the literature are far less than 1 km (Aram et al. 2019).

180

181 Finally, we used temperature and wind speed and direction measured at the top of the Eiffel  
182 Tower (287 m AGL) to monitor conditions at a height generally located in the nocturnal urban  
183 boundary layer.

184

#### 185 **i) Doppler Wind Lidar**

186 A Doppler Wind Lidar (DWL) is used in this study to deduce the intensity of vertical turbulent  
187 mixing. The Vaisala DWL WindCube Scan 400 was installed at 90 m above ground level (AGL)  
188 at the top of the Zamansky Tower located on the campus of Sorbonne University in the 5<sup>th</sup>  
189 district of Paris (QUALAIR atmospheric station location shown on Fig. 1; <https://qualair.fr/>) to  
190 measure horizontal wind and vertical velocity. In this study, we use vertical-stare mode of the  
191 DWL to derive vertical velocity variance ( $\sigma_w$ ) profiles. Each variance profile is calculated from  
192 300 vertical velocity profiles collected during a 5-min period (one profile per second). Vertical  
193 velocity variance profiles are available every 30 minutes. Due to the installation setup, the  
194 first gate available for deriving the vertical velocity variance is at 240 m AGL.

195

#### 196 **ii) Windsond**

197 A Windsond is a lightweight sonde (12 grams) manufactured by Sparv Embedded, Sweden  
198 (<https://sparvembedded.com/products/windsond>). This instrument, packaged in a styrofoam  
199 cup, records pressure, temperature, and relative humidity approximately every second.  
200 Latitude and longitude are determined using an onboard GPS receiver. The S1H3 windsond  
201 model calculates wind speed and direction independently from latitude and longitude,  
202 utilising the GPS signal. Thanks to its lightweight design, the balloon size is somewhat

Supprimé:

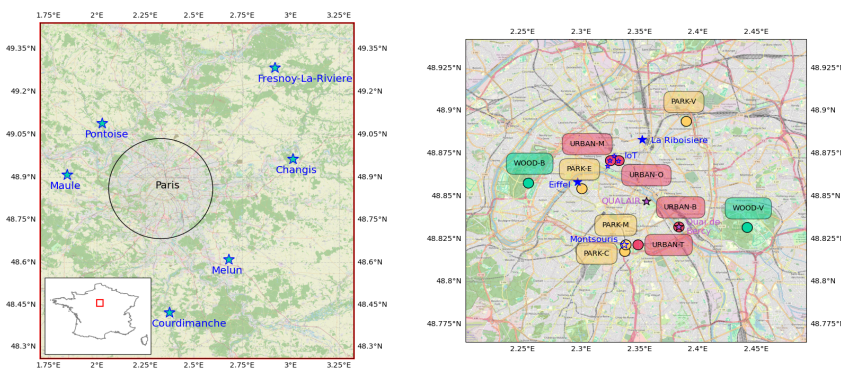
Supprimé: 238

205 equivalent to a "party balloon", requiring about 50 L of helium, and making it particularly  
206 suitable for probing the lower parts of the troposphere.

207 For each IOP, three profiles were produced using windsonds to monitor evening cooling at  
208 16, 20 and 00 UTC. The 16 UTC profile corresponds to conditions of maximum daytime  
209 temperatures. The 20 UTC profile samples conditions about 1 hr after sunset, while the 00  
210 UTC profile is performed in conditions close to the maximum nighttime UHI.

211 Corrections have been applied to raw data as follows. Before the windsond is released, the  
212 temperature and humidity sensors are not ventilated. Unventilated data (before launch) are  
213 thus carefully compared with the first points of the ventilated profile, and corrected if  
214 necessary. As the temperature and humidity sensors are outside the styrofoam cup, the  
215 windsond is subject to the influence of solar radiation during the day. A daytime overheating  
216 on the order of about +1°C was observed by comparing those profiles with data collected by  
217 Vaisala RS41-SGP radiosondes launched at the same time the URBAN-B location (see  
218 Appendix 1). A correction of -1°C was therefore applied across the entire profile for  
219 windsonde data at 16 UTC. No radiative correction is applied at 20 and 00 UTC.

220



221  
222 Figure 1: (left) Locations of the six weather stations contributing to the rural setting  
223 reference. (right) Locations of fixed weather stations in Paris city (blue stars) and of  
224 windsonde and radiosonde launch sites in urban woods (green dots WOOD), urban  
225 parks (yellow dots PARK) and built-up areas (red dots URBAN). © OpenStreetMap  
226 contributors 2023. Distributed under the Open Data Commons Open Database  
227 License (ODbL) v1.0.

228



229  
230

## 231 2.2 Sampling methodology

232

233 Our study focuses on evening temperature evolution at various locations across the Paris  
234 region under predominantly cloud free conditions. The cloud cover fraction is derived on an  
235 hourly basis using a Lufft CHM15k automatic lidar ceilometer located at the SIRTA observatory  
236 (Haeffelin et al. 2005) and a second one located at the QUALAIR atmospheric station. Evening  
237 cloud-free conditions are defined as a cloud fraction less than 20% for each hour between 16  
238 and 00 UTC. In the period June-August 2022, 54 days are classified as “evening cloud-free  
239 conditions”. On average this period is characterized by a positive temperature anomaly and  
240 near-zero precipitation anomaly (not shown).

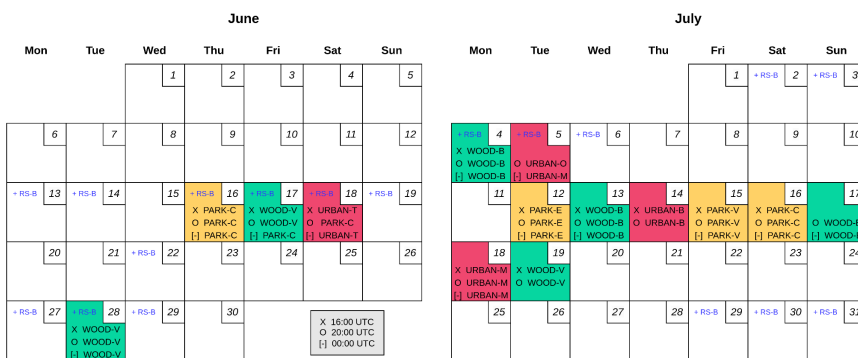
241

242 The 14 intensive observation days were selected to focus predominantly on warm to hot  
243 daytime conditions followed by cloud free nights. Two heat wave events were covered with  
244 intensive observations, the first one on 16-18 June and the second one on 12-19 July.

245 Windsond launch sites were classified in three types of settings i.e., urban woods, urban parks  
246 and built-up areas. Two urban woods, located East of the city (Bois de Vincennes, 995 ha;  
247 WOOD-V in Fig. 1) and West of the city (Bois de Boulogne, 845 ha; WOOD-B), are mostly  
248 wooded, including open lawns, small lakes, buildings and roads. Three urban parks of  
249 comparable size were selected to sample different neighbourhoods of the city. One is located  
250 south of the city centre (Cité Universitaire about 32 ha with 50% green space and 50%  
251 housings and small roads, located across the street from Montsouris Park; PARK-C), the  
252 second one is West of the city centre (Eiffel Tower park, 24 ha, predominantly trees and open  
253 lawns; PARK-E), and the third one is Northeast of the city centre (La Villette Park, 55 ha  
254 including 30 ha of green space and 25 ha of built-up areas; PARK-V). The three selected urban  
255 parks differ however in terms of vegetation type (species; fractions of trees, shrubs and grass)  
256 and also in terms of irrigation practices and hence soil moisture. These differences and their  
257 effects are not accounted for in this study. Windsonds were also launched from four built-up  
258 areas: one in the 13<sup>th</sup> district close to Montsouris Park (URBAN-T in Fig 1.), two in the 9<sup>th</sup>  
259 district close to the Opera IoT stations (URBAN-M and URBAN-O), and one in the 12<sup>th</sup> district

260 next to the radiosonde launch site (URBAN-B). For the June 3-day heat wave, we sampled one  
 261 park, one wood and one built-up site. For the July heat wave, we were able to sample the  
 262 three parks, two woods and two built-up sites. Launch sites are shown in Fig. 1 and IOP dates  
 263 and launch locations are shown in Table 1.

264  
 265  
 266



267  
 268 Table 1: Dates of the 14 IOP with location and time of launch of windsonds.  
 269 Locations are shown in Fig. 1. +RS-B indicates that radiosondes were launched from the  
 270 URBAN-B location at the same time as the windsonds. The colour indicates the location type  
 271 for each day as Urban Park (Yellow), Urban Wood (Green), or built-up setting (Red).

272  
 273  
 274

### 275 3 - Urban park cooling effect in relation to regional- 276 scale UHI

277 The cooling effect intensity of an urban park is derived as the temperature difference between  
 278 a representative built-up neighbourhood and the green infrastructure where we expect  
 279 cooler nocturnal conditions. In our study, the cooling effect intensity of the Montsouris Park  
 280 is computed, on an hourly mean basis, as the deficit of temperature measured in the park  
 281 relative to the air temperature measured in the built-up setting (at Lariboisière and Opera

282 sites - see detailed definition of locations in Section 2). As park cooling effect intensity is  
283 reported to be highly variable, we study this variability as a function of the nocturnal UHI in  
284 the Paris region, which represents the regional-scale temperature contrasts between the  
285 same built-up environment and the vegetated rural reference. The study covers summer 2022  
286 focusing on the 54 evening periods with cloud-free conditions (defined in Section 2).  
287

### 288 3.1 Summertime urban park cooling effect variability

289 The regional UHI is known to be dependent on both cloud-cover fraction and wind speed.  
290 Here we focus on cloud-free nights, for which the UHI has been found to be proportional to  
291 the inverse of the square-to-third root of the wind speed (e.g. Morris et al. 2001). Cespedes  
292 et al. (2024) has also shown that the strongest UHI intensities are found for very low vertical  
293 velocity variance values, measured above the urban canopy, and that UHI decreases as  
294 vertical velocity variance increases.

295 Fig. 2 presents median nocturnal cooling intensity of the Montsouris Park (a 15-ha urban park)  
296 against the median nocturnal regional UHI and median vertical velocity variance computed  
297 over the 19-02 UTC time interval for each night. A K-means clustering method based on the  
298 three variables is used to identify different regimes. The figure reveals three different  
299 regimes. In conditions of strongest UHI (6-10°C), we find a group of days where the park  
300 cooling effect intensity ranges 2-5°C. In this regime, the vertical velocity variance is very low  
301 with median nocturnal values ranging from 0.02 to 0.1 m<sup>2</sup>s<sup>-2</sup>. In these conditions, urban park  
302 cooling intensity relative to the built-up environment shows a strong variability, but is on  
303 average half the regional UHI intensity. In conditions of weak UHI intensity (2-4°C), the park  
304 cooling effect is close to 1°C, while the vertical velocity variances are high (greater than 0.25  
305 m<sup>2</sup>s<sup>-2</sup>). In this regime, intra-urban temperatures are most homogeneous and urban-rural  
306 contrasts are minimal, which is likely due to significant advection. In between, we find a  
307 number of days where the urban park cooling effect remains limited (1-2°C), while the urban-  
308 rural temperature contrasts are significantly stronger (4-8°C), by a factor of about four. In  
309 these conditions, we find that the vertical velocity variances range between 0.1 and 0.2 m<sup>2</sup>s<sup>-2</sup>.  
310 For those days, the rural environment around the city cools very efficiently, while the urban  
311 setting remains hot with little intra-urban contrasts.

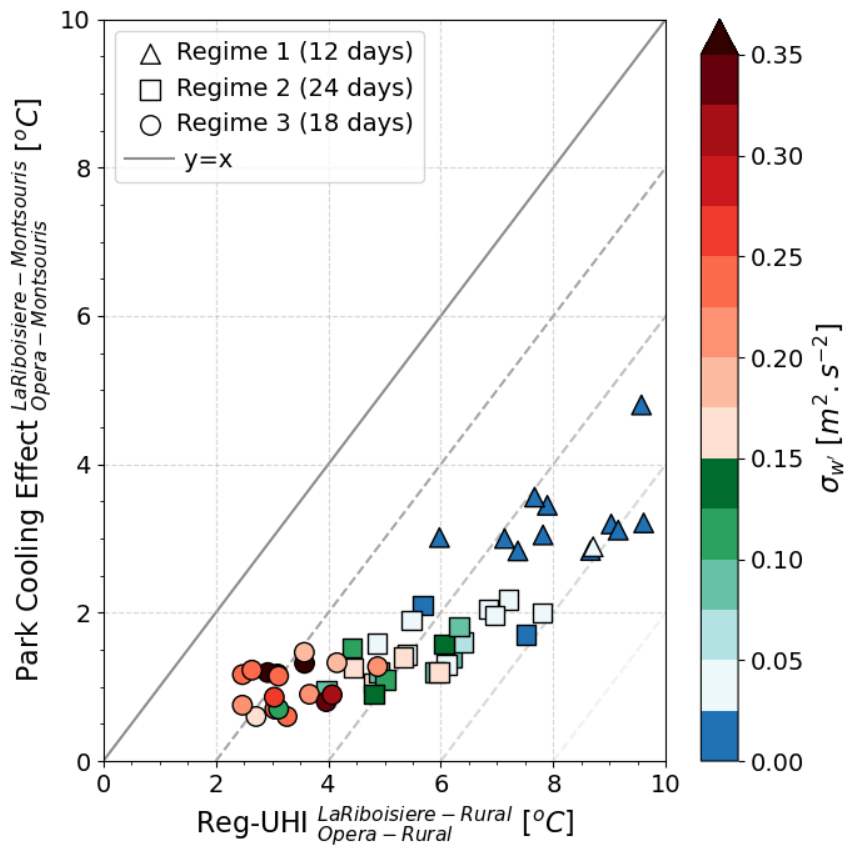
312 In summary, we can state that:

- 313 ● Conditions of strong park cooling intensity combined with strong regional UHI  
314 intensity occur in a regime of low vertical velocity variance. This regime will be referred  
315 to as the stagnant regime in the rest of the paper,
- 316 ● Conditions of moderate park cooling intensity combined with strong regional UHI  
317 intensity occur in a regime of moderate vertical velocity variance (referred to as the  
318 intermediary regime).
- 319 ● conditions of weak park cooling intensity combined with weak regional UHI intensity  
320 occur in a regime of high vertical velocity variance (referred to as the turbulent  
321 regime).

322 Based on these findings, several questions arise. What processes drive the evening cooling in  
323 the urban park in these different conditions? What is responsible for the different urban park  
324 cooling effects that we find for low, moderate and high vertical velocity variance?

325

326



327  
 328 Figure 2. Nocturnal urban park cooling effect intensity against regional-scale UHI intensity and  
 329 vertical velocity variance (color scale), derived from 8 hours of measurements (median 19-02  
 330 UTC values) for the 54 cloud-free evenings.  
 331

### 332 3.2 Urban park cooling effect variability in a heatwave period

333  
 334 To better understand factors affecting the variability in nocturnal temperature contrasts  
 335 between urban parks and the built-up settings, we focus next on an eight-day event (12-19

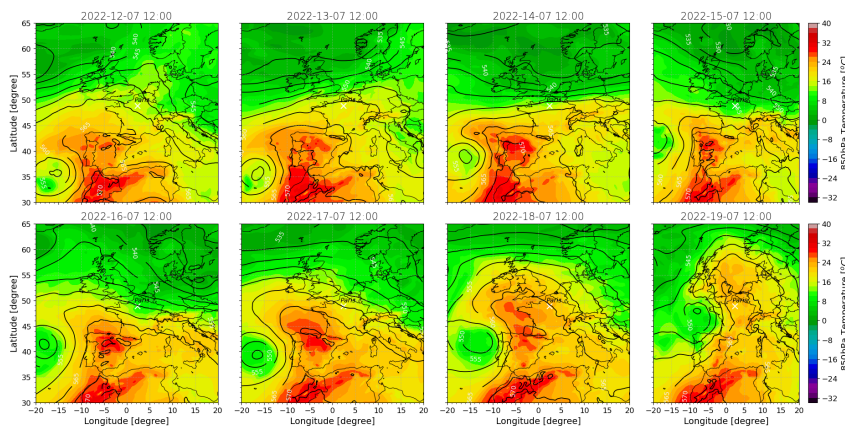
336 July 2022) that is characterised by extreme daytime temperature (peak values approaching  
337 40°C on several days) and a set of diverse evening cooling patterns.

338

339 This period is characterised by a powerful anticyclonic axis between Morocco, France and the  
340 British Isles, which gradually warmed the air (Fig. 3). A secondary low-pressure system located  
341 between the Azores and Portugal moved towards the Bay of Biscay, strengthening advection  
342 of particularly hot air from the Iberian Peninsula. This contributed to the intensification of a  
343 heatwave over the European continent, with an extreme peak over the Paris region on 19  
344 July. As it moved north-eastwards over France, this low pressure system advected cooler  
345 oceanic air from the west, causing temperatures to fall and progressing eastwards with  
346 thunderstorm activity. During the heatwave, the 850 hPa temperature exceeded 20°C, while  
347 on standard summer days, it is closer to 10°C.

348

349



350

351 Figure 3: Synoptic overview from 12 to 19 July 2022 based on ERA5 reanalysis. The colour  
352 bar represents temperature at 850 hPa, and the contours represent the geopotential height  
353 difference between 500 hPa and 1000 hPa (dam).

354

355 Figure 4 shows the temporal evolution of near-surface atmospheric conditions during the  
356 eight-day period. Figure 4a compares the 2-m air temperature measured in Opera built-up  
357 setting, Montsouris urban park, and the rural reference setting. The regimes identified in  
358 Section 3.1 are also shown for each night. Figure 4b presents the rate of change of

Supprimé: the

Supprimé: 19

361 temperature over time at the three locations. Figure 4c shows the temperature differences  
362 between the built-up site and the urban park and the rural setting, respectively. Figure 4d  
363 presents the wind speed and direction measured at the Montsouris urban park 25 m AGL and  
364 Fig. 4e shows the vertical velocity variance measured at 240 m AGL.

365  
366 The eight-day period is characterised by a first heat wave on July 12 and 13 (stagnant regime),  
367 due to the advection of hot air shown in Fig. 3, with maximum temperature exceeding 35°C,  
368 followed by three days of more moderate heat on July 14, 15, and 16 (intermediary and  
369 turbulent regimes, maximum temperature at or below 30°C and minimal temperatures in the  
370 built-up environment less than 20°C). A second, more intense, advection of hot air occurs the  
371 following three days on July 17, 18, and 19 (stagnant regime) with daytime maximum  
372 temperatures exceeding 35°C. Figure 4a shows that the daytime maximum temperatures  
373 (between 16 and 17 UTC) in the built-up, urban park and rural settings are close, within 1°C  
374 of each other. Conversely, night-time minimal temperatures (between 03 and 04 UTC) differ  
375 by 4-10°C between the built-up and rural settings with significant day to day variations (Figure  
376 4c).

377  
378 Figure 4b shows positive heating rates from sunrise until about one hour before sunset. Peak  
379 heating rates reach 2-3°C/hr, but are on average near 1°C/hr. One hour before sunset,  
380 temperature changes become negative (cooling). We observe a two-phase cooling consistent  
381 with earlier findings reported in the literature (e.g. Holmer et al. 2013). The first phase lasts  
382 from 16 to 21 UTC. It is characterised by large changes in cooling rate reaching maximum  
383 values near 19-20 UTC and with differences of up to 2°C/hr between built-up, urban park, and  
384 rural cooling rates (on 12/07, 17/07 and 18/07). The second phase starts after 21 UTC and  
385 lasts until sunrise or about 04 UTC. It is characterised by more moderate cooling rates of  
386 typically less than -1°C/hr and by virtually no contrasts between built-up, park and rural  
387 settings.

388  
389 In the evening, air temperature cooling in the urban canopy is driven by a combination of  
390 processes, including radiative cooling of the surfaces and the air (through radiative flux  
391 divergence), turbulent heat exchange (through sensible and latent heat fluxes), release of  
392 heat from the ground (storage heat flux), vertical mixing of air, and advection (Oke 2017).

393 These processes are known to depend on the surface types and properties (albedo, emissivity,  
394 heat capacity, soil moisture), the 3-D canopy structure (sky view factor), the city morphology,  
395 anthropogenic heat emissions, the spatial distribution of surface types (urban to rural surface  
396 gradients), and synoptic-scale weather conditions (wind, clouds). According to Steeneveld et  
397 al. (2006), atmospheric static stability and mesoscale dynamics affect the relative contribution  
398 of the radiative and turbulent processes. When the vertical turbulent mixing is low, turbulent  
399 heat fluxes are weak, hence air temperature cooling is dominated by radiative flux divergence,  
400 partially compensated by the storage heat flux.

401

402 This is consistent with cooling rates shown in Fig. 4b. In the rural setting and in the urban park,  
403 where the storage heat flux is low, the largest cooling rates (peaking at  $-3^{\circ}\text{C}/\text{hr}$  and  $-2^{\circ}\text{C}/\text{hr}$   
404 respectively) are observed in conditions of low vertical velocity variance (Fig. 4e), on the  
405 evenings of 12/07, 17/07 and 18/07 (stagnant regime). In the built-up area, the radiative  
406 cooling is partially compensated by a stronger ground heat flux. On nights with moderate to  
407 high vertical velocity variance, radiative flux divergence is reduced and also compensated by  
408 sensible and latent heat flux releases, which leads to lower cooling rates in both urban park  
409 and rural settings. The excess of urban-park cooling compared to the built-up environment  
410 lasts four to six hours (from 18 to 00 UTC) as is the case for the rural surface.

411

412 The contrasts in cooling rates between the built-up environment, the urban park and the rural  
413 settings can explain the large variability in nocturnal park cooling effect and regional-scale  
414 UHI intensities shown in Fig. 4c. On the three nights with lowest wind speed ( $<2\text{ m s}^{-1}$ , Fig. 4d)  
415 and lowest vertical velocity variance ( $<0.05\text{ m}^2\text{ s}^{-2}$ ), that is on 12-13/07, 17-18/07 and 18-  
416 19/07 (stagnant regime), the maximum regional UHI intensity exceeds  $8^{\circ}\text{C}$ , while the  
417 maximum park cooling effect reaches nearly  $4^{\circ}\text{C}$ . On those nights, in the built-up  
418 environment, the air temperature cools by  $7-9^{\circ}\text{C}$  from sunset to sunrise, while the urban park  
419 cools an extra  $3-4^{\circ}\text{C}$ , and the rural setting an additional  $3-4^{\circ}\text{C}$ . On the night with moderate  
420 wind speed ( $3-4\text{ m s}^{-1}$ ) and moderate vertical velocity variance, 15-16/07(intermediary  
421 regime), the regional UHI peaks near  $6^{\circ}\text{C}$ , while the park cooling effect reaches about  $2^{\circ}\text{C}$ . On  
422 this night, the air temperature cools by about  $10^{\circ}\text{C}$  from sunset to sunrise in the built-up  
423 environment, while the urban green infrastructure cools an extra  $2^{\circ}\text{C}$ , and the rural setting an  
424 additional  $3-4^{\circ}\text{C}$ . On the nights of 14-15/07 and 16-17/07 (turbulent regime), the wind speed

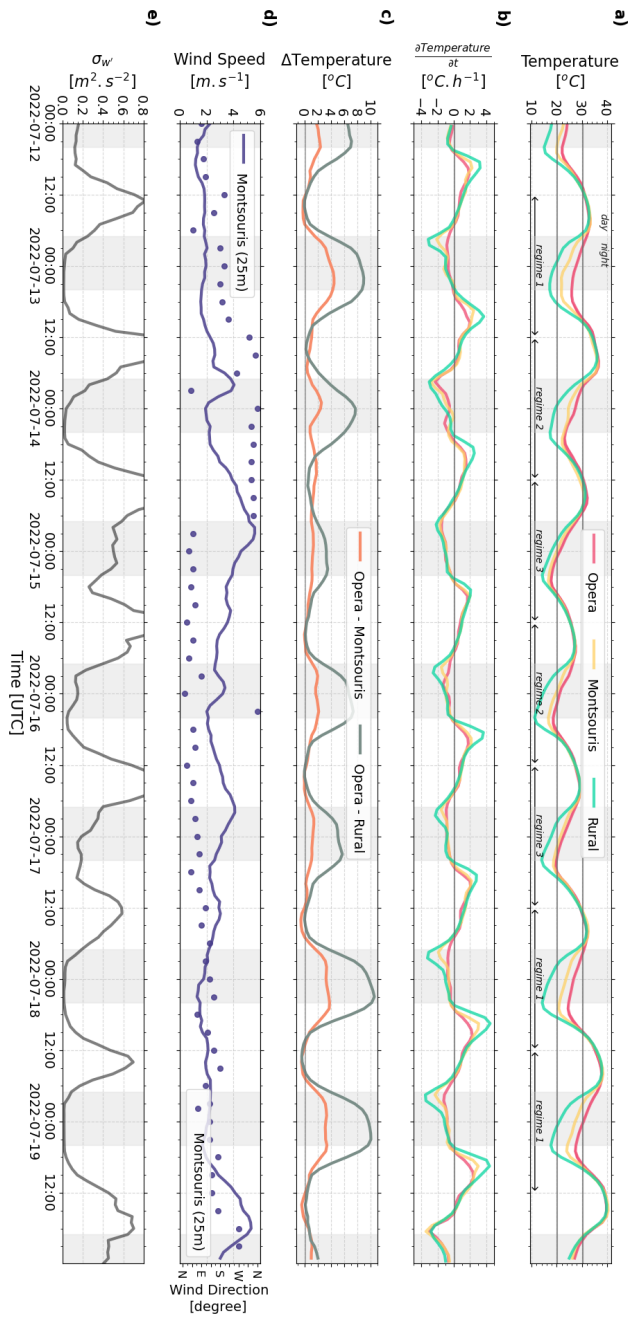


425 exceeds  $4 \text{ m s}^{-1}$  and the park cooling effect reaches just  $1^\circ\text{C}$ , while the maximum regional UHI  
426 intensity is about  $4^\circ\text{C}$ .

427

428 The analysis of the 12-19 July period confirms the results shown in Fig. 2. Different regimes  
429 exist that influence park cooling effect and regional UHI intensities. In particular, during nights  
430 with very low wind speeds, the air above the urban park cools significantly more (up to  $4^\circ\text{C}$ )  
431 than in our reference built-up environment. To better understand the processes and  
432 conditions that affect these nocturnal intra-urban cooling contrasts we will investigate the  
433 dynamics and thermodynamics of the urban boundary layer over green infrastructures of  
434 different sizes in the following section.

435



437 Figure 4: near-surface temperature and nighttime turbulence regimes (a) and cooling rate (b)  
438 measured in a built-up environment (Paris Opera district), an urban park (Montsouris park,  
439 15-ha), and the average of 6 rural locations around Paris; Urban park cooling effect (Opera-  
440 Montsouris temperature difference) and regional-scale UHI (Opera-Rural temperature  
441 difference) (c); wind speed and direction measured at Montsouris Park 25 m AGL (d); and  
442 vertical velocity variance measured in Paris city centre 240 m AGL. 12-19 July 2022; during  
443 that week, the sun sets at about 19 UTC and rises at about 04 UTC.  
444

Supprimé: 238

## 445 4) Evening cooling in and above urban parks and 446 urban woods

447  
448 In this section, we focus on four different nights to study the characteristics of evening cooling  
449 mechanisms above urban green spaces considering dynamics of the urban boundary layer for  
450 the three turbulence regimes. For each evening period (16-00 UTC), we analyse time series of  
451 near-surface temperature, humidity, and wind measured in the built-up environment, urban  
452 green infrastructures, and rural settings. To investigate the relative role of relevant cooling  
453 mechanisms, i.e. radiative cooling of the surfaces, radiative cooling of the air through  
454 radiative flux divergence, turbulent heat exchange, vertical mixing, and advection, it is helpful  
455 to quantify conditions in the urban boundary layer. Therefore, in order to assess the relative  
456 roles of surface-driven and atmospheric-driven processes, the conditions measured at the  
457 surface are complemented by the analysis of the observations at the top of the Eiffel Tower  
458 (287 m AGL), as well as vertical profiles of meteorological variables obtained from windsound  
459 profile measurements.  
460

### 461 4.1 Stagnant regime: strong park cooling effect combined with 462 strong UHI intensity

463

465 Here we focus on two nights that show the strongest park cooling effect intensity and most  
 466 significant UHI intensity, classified as stagnant regime, i.e. 12-13/07 and 17-18/07. Both  
 467 selected nights occur in high-pressure synoptic conditions with meso-scale subsidence over  
 468 the region. Hot air advection driven by a secondary pressure low located west of the Iberian  
 469 Peninsula led to 850 hPa temperatures near 20°C. Both nights are characterised by very warm  
 470 conditions over the preceding daytime period with daily maximum air temperatures  
 471 exceeding 32°C (see Fig.s 5a, 6a). Strong regional-scale UHI and park cooling intensities are  
 472 due to sharp contrasts in peak cooling rates (Fig.s 5b and 6b) between built-up, park and rural  
 473 settings that last for 4-6 hours. On both 12/07 and 17/07, an evening cooling (16-00 UTC) of -  
 474 5°C, -9°C and -14°C is documented in the built-up, urban park and rural settings, respectively,  
 475 as shown in Table 2.  
 476

Regimes	16-00 UTC cumulative temperature change [°C] (average cooling rate [°C/h])		
	Opera	Park	Rural
<b>Stagnant Regime :</b> <b>Strong park cooling</b> <b>effect and strong UHI</b> <b>intensities</b>	-5.1 (-0.6)	-9.1 (-1.1)	-14.0 (-1.8)
<b>Intermediary Regime:</b> <b>Moderate park cooling</b> <b>effect and strong UHI</b> <b>intensities</b>	-5.9 (-0.7)	-7.6 (-0.9)	-12.6 (-1.6)
<b>Turbulent Regime:</b> <b>Weak park cooling</b> <b>effect and low UHI</b> <b>intensities</b>	-9.6 (-1.2)	-9.4 (-1.2)	-13.1 (-1.6)

477 Table 2: 16-00 UTC cumulative evening temperature change and average cooling rate for the  
 478 three types of turbulence regimes.

479

480 The relatively strong cooling rate in the urban park compared to the built-up settings suggests  
481 that the surface-driven processes (i.e. radiative cooling and/or turbulent latent heat fluxes)  
482 are rather efficient on those nights. In comparison, the air temperature at the top of the Eiffel  
483 Tower peaks generally around 18 UTC, i.e. about 2 hr later than near the surface at values 2-  
484 3°C colder than the near-surface air temperature (Figs 5a and 6a). After 18 UTC, the air starts  
485 to cool with a rate of around -0.35°C/hr, which is nearly half the value of the near-surface  
486 cooling rate measured in the built-up environment (Figs 5b and 6b). Hence, the air at 287 m  
487 AGL is only moderately affected by the processes that cool the air close to the surface. This is  
488 the first evidence of decoupling between the urban canopy layer (UCL) and the air above, and  
489 the decrease in static instability in the urban boundary layer (UBL).

490

491 Further evidence of this decoupling due to static stability in the UBL can be found in the wind  
492 speed measurements. Figures 5c and 6c show the time series of wind speed at 10 m AGL at  
493 the Melun rural site, at 25 m AGL in the Montsouris urban park and at 287 m AGL at the Eiffel  
494 Tower, for 12/07 and 17/07, respectively. A comparable temporal evolution of wind speed  
495 can be observed in the evening hours on both days. During the afternoon, the wind speed at  
496 both the urban park and the rural site are consistent (about 2-4 m s<sup>-1</sup> and within 1-2 m s<sup>-1</sup> of  
497 each other). After about 18 UTC, the wind speed at 287 m AGL increases rapidly to reach 8-  
498 10 m s<sup>-1</sup> before 00 UTC, while the rural and urban park wind speed remains low at or below 2  
499 m s<sup>-1</sup>, i.e. often lower than during daytime. This is a second evidence that after sunset,  
500 decoupling conditions occur between the surface layer and the air above.

501

502 Figures 5 and 6 g and h show vertical profiles of wind speed and direction derived from  
503 windsound profiles launched at 16, 20 and 00 UTC over an urban park (PARK-E; Fig. 1) on 12/07  
504 and a large urban wood (WOOD-B; Fig. 1) on 17/07, respectively. Both IOPs are characterised  
505 by easterly winds with relatively little wind direction evolution in the evening. During daytime  
506 (16 UTC), the wind speed is moderate (2-4 m s<sup>-1</sup>) in the first 700 m of the atmospheric  
507 boundary layer. The windsounds launched after sunset (near 20 UTC) reveal in both cases low  
508 near-surface wind speed (1.5-2.0 m s<sup>-1</sup>) that gradually increases with height (consistent with  
509 results described in the previous paragraph). A 3 m s<sup>-1</sup> wind shear can be observed on 17/07  
510 between the surface and 200 m AGL. The wind shear is not as strong on 12/07, possibly

511 because the profile was measured 45 min earlier than on the other day. This wind shear is a  
512 signature of the stabilisation of the atmosphere that inhibits the vertical transfer of  
513 momentum and hence decouples the air aloft from surface drag effects, allowing the wind  
514 speed to increase aloft (e.g. Barthelemie et al. 1996).

515  
516 The windsonds launched at 00 UTC reveal even stronger windshear between surface and 200  
517 m AGL, with maximum wind speed of around  $6.5 \text{ m s}^{-1}$  on both nights near 300 m AGL and a  
518 decreasing wind speed above. This vertical structure is known as a low-level jet (LLJ), a  
519 condition that occurs frequently on summer nights above Paris according to Céspeles et al.  
520 (2024). Their work has shown that very low altitude LLJs are associated with low levels of  
521 turbulence, due to the fact that they form in a statically stable atmosphere that inhibits  
522 mechanically induced turbulence.

523  
524 To characterise the importance of vertical mixing as a potential means for heat transfer  
525 between the UCL and the nocturnal urban boundary layer, we use Doppler wind lidar  
526 measurements to derive time series of vertical velocity variance (Figs 5d and 6d). During the  
527 convective period of the two IOPs, the vertical velocity variance typically exceeds  $0.5 \text{ m}^2 \text{ s}^{-2}$ . It  
528 then decreases rapidly around sunset. At 20 UTC, the values have dropped to less than  $0.05$   
529  $\text{m}^2 \text{ s}^{-2}$  on both 12/07 and 17/07, and remain very low all night. This confirms the very low  
530 vertical turbulent mixing in the UBL on both nights. It should be noted that in the stagnant  
531 regime, the vertical velocity variance values are very low (less than  $0.05 \text{ m}^2 \text{ s}^{-2}$ ) throughout  
532 the LLJ layer that extends from 240 to about 500 m AGL or more (not shown). Hence even  
533 though vertical velocity variance is not constant with height and the measurement height  
534 (240 m AGL) is close the top of the UBL, we conclude that the vertical velocity variance value  
535 at 240 m AGL is representative of the nocturnal urban boundary layer turbulence regime.

536  
537 To characterise the role of vertical radiative flux divergence in the atmospheric boundary  
538 layer, and to better understand the relative importance of surface-driven vs atmospheric-  
539 driven processes, we analyse the vertical structure of temperature and its temporal evolution.  
540 In the Eiffel Tower urban park (PARK-E), we find that near-surface temperatures measured by  
541 the windsond on 12/07 are consistent with temperatures recorded by the Montsouris urban  
542 park surface station (yellow circles in Fig. 5a). At 20 UTC, we observe a  $1^\circ\text{C}$  temperature

Mis en forme : Police :12 pt

543 inversion between the surface and 50 m AGL (Fig. 5f). Above the inversion, the temperature  
544 decreases adiabatically by about  $-1^{\circ}\text{C}/100\text{ m}$  so that the potential temperature is nearly  
545 constant in a statically neutral layer between 50 and 700 m (Fig. 5f). At 00 UTC, the surface-  
546 based inversion has become stronger ( $\Delta T_{\text{air}} = 2.5^{\circ}\text{C}$  and  $\Delta \theta_{\text{air}} = 3.0^{\circ}\text{C}$  between the surface and  
547 50 m AGL), and two elevated inversions have formed near 100 and 200 m AGL (Fig. 5f, g), with  
548  $\Delta \theta_{\text{air}} = 0.5^{\circ}\text{C}$  followed by a statically stable layer with a  $+0.2^{\circ}\text{C}/100\text{ m}$  lapse rate (Fig. 5g).

549

550 In the urban wood (WOOD-B), near-surface temperatures measured by the windsound on  
551 17/07 are close to temperatures measured in the rural settings (green circles in Fig. 6a). With  
552  $3.5^{\circ}\text{C}$  decrease over 50 m, the surface-based temperature inversion at 20 UTC (Fig. 6e) is  
553 already stronger than the inversion observed at 00 UTC over PARK-E on 12/07. Above the  
554 inversion, the temperature decreases adiabatically (Fig. 6e, f) and the potential temperature  
555 profile confirms that the stable wood UBL is capped by a neutral layer above. At 00 UTC, the  
556 surface-based inversion strengthens and extends aloft ( $\Delta T_{\text{air}} = 5.0^{\circ}\text{C}/100\text{ m}$  ;  $\Delta \theta_{\text{air}} = 6^{\circ}\text{C}/100$   
557  $\text{m}$ ), followed by an elevated inversion near 250 m AGL (Fig. 6f, g). The potential temperature  
558 profile is stable between 100 and 300 m AGL ( $+1.0^{\circ}\text{C}/100\text{ m}$ ) and moderately stable  
559 ( $+0.2^{\circ}\text{C}/100\text{ m}$ ) above (Fig. 6g).

560

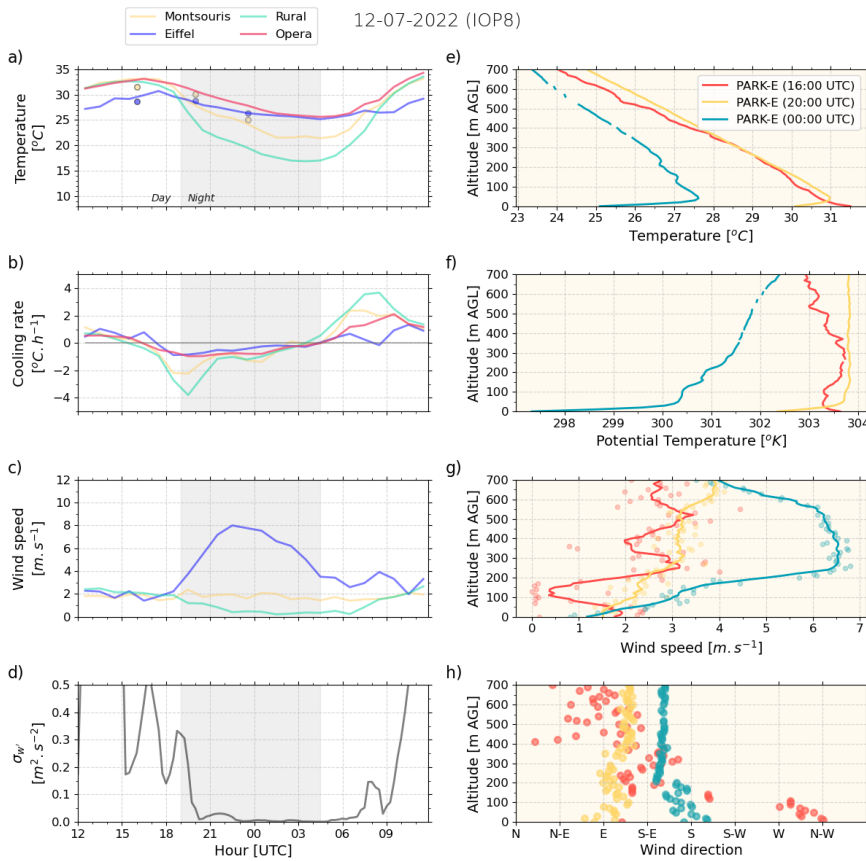
561 These elevated inversions observed both over the urban park and urban wood could be  
562 formed through localised radiative cooling, subsidence and/or advection of statically stable  
563 rural air that is commonly observed above nocturnal UBL (e.g. Tsiringakis et al. 2022). Elevated  
564 inversions in nocturnal UBLs are simulated and studied extensively in Martilli (2002). The drag  
565 and turbulent kinetic energy production induced by the urban structure increases with  
566 increasing wind speed. Vertical mixing of potential temperature leads to a local minimum of  
567 temperature at the location of maximum turbulence through a negative turbulent heat flux.  
568 According to Martilli (2002), the net result of the vertical turbulent transport is to heat the  
569 layer below the base of the inversion and to cool the inversion layer. Cooling of the inversion  
570 layer (roughly between 200 and 300 m AGL) is clearly seen on the both windsound temperature  
571 profiles measured at 00 UTC.

572

573 We can conclude that the conditions of stagnant regime, combining strong park cooling  
574 effects and strong UHI intensities, are associated with a significant surface-based inversion

575 that leads to the decoupling not only of the rural nocturnal boundary layer from the residual  
 576 layer but also between the urban boundary layer and the neutral layer above. The strong  
 577 stratification suppresses nearly any turbulent vertical motion so that the UBL height is rather  
 578 shallow - even below the top of the Eiffel Tower. As the flow is no longer subject to surface  
 579 drag, a regional low-level jet forms that likely advects rural, statically stratified air over the  
 580 UBL, which can influence the development of elevated inversions. The strong stratification in  
 581 the park internal UBL is the result of cooling dominated by radiative flux divergence due to  
 582 low turbulent mixing.

583  
 584

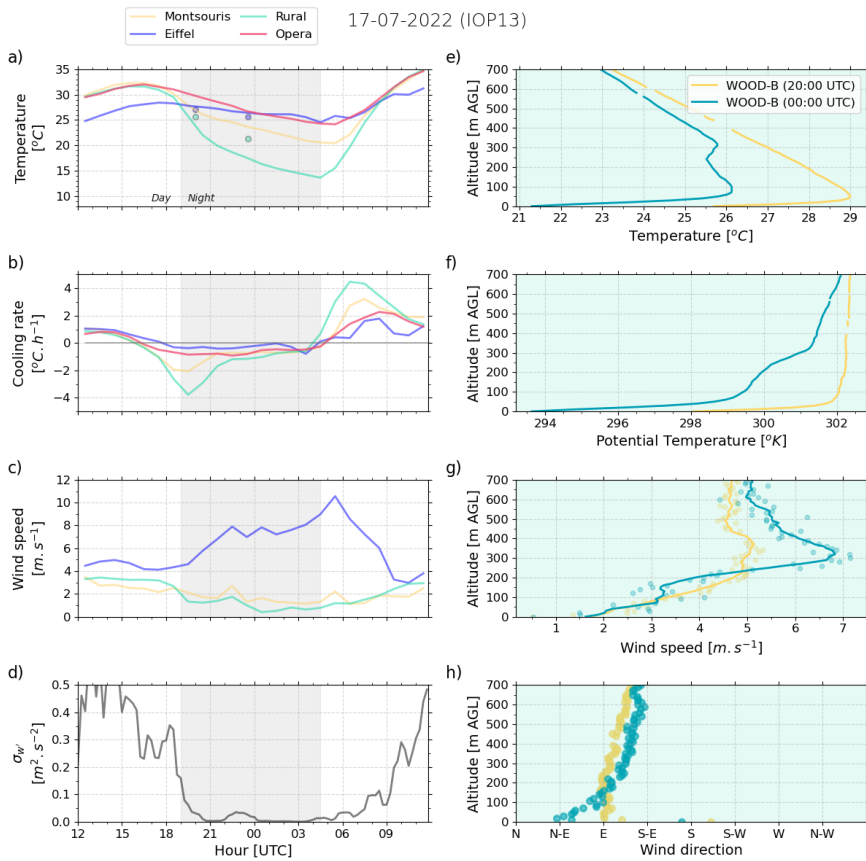


585



586 Figure 5: Time series and windsonde profile measurements for July 12, 2022. a-d) Time series  
 587 measurements from 12 UTC to 12 UTC (D+1). a) Temperature at Montsouris Park, Rural  
 588 settings, Opera (built-up) and top of Eiffel Tower. The coloured dots show the temperature  
 589 measured by windsonds at 16, 20, and 00 UTC, respectively at park level and at the height of  
 590 the Eiffel Tower (287m AGL). b) Cooling rate at Montsouris, Rural, Opera and Eiffel Tower. c)  
 591 Wind speed at Montsouris, Rural, and Eiffel Tower. d) Vertical velocity variance from DWL at  
 592 240 m AGL at QUALAIR-SU site. e-h) Vertical profiles from radiosonde measurements  
 593 released in PARK-E at 16, 20, and 00 UTC, respectively. e) Temperature profile. f) Potential  
 594 temperature profiles. g) Wind speed profiles. h) Wind direction profiles.

Supprimé: 238



596  
 597 Figure 6: same as Fig. 5 for July 17, 2022.

598  
 599

601  
602  
603  
604  
605  
606  
607  
608  
609

## 610 4.2 Intermediary regime: moderate park cooling effect 611 combined with strong UHI intensity

612

613 The evening of 15-16/07, compared to those discussed in Section 4.1, is characterised by  
614 weaker cooling between 16 and 00 UTC in the rural setting and urban park, and stronger  
615 cooling in the built-up environment, as shown in Table 2. It is classified in the intermediary  
616 regime. Cooling peaks near  $-3^{\circ}\text{C}/\text{hr}$  in the rural setting and  $-1.5^{\circ}\text{C}/\text{hr}$  in urban park, which is  
617 slightly less than for the cases of Section 4.1 (Fig. 7b). For this regime, the nocturnal near-  
618 surface wind only decreases in the rural setting while it increases in the urban park after 21  
619 UTC as the wind aloft picks up (Fig. 7c) which indicates that vertical momentum transfer is  
620 less inhibited above the urban surface. Figure 7d shows that the vertical turbulent mixing  
621 remains above  $0.1 \text{ m}^2 \text{ s}^{-2}$  after sunset and increases to  $0.2 \text{ m}^2 \text{ s}^{-2}$  during the evening which  
622 confirms that the UBL remains turbulent during the night.

623

624 The windsound profiles carried out in the La Villette urban park (PARK-V on Fig. 1), for which  
625 the vegetated area is comparable to that of the Montsouris urban park, reveal at 20 UTC a  
626 slight surface-based inversion with a neutral layer above, while at 00 UTC under brisker  
627 turbulent mixing the UBL remains near-neutral from the ground up to a temperature  
628 inversion near 300 m AGL. It is then likely that the UBL remains neutral due to sensible heat  
629 flux originating from the hot surface combined with turbulent mixing and from the  
630 temperature inversion above. Again, a clear low-level jet with peak horizontal velocity  $> 9 \text{ m}$

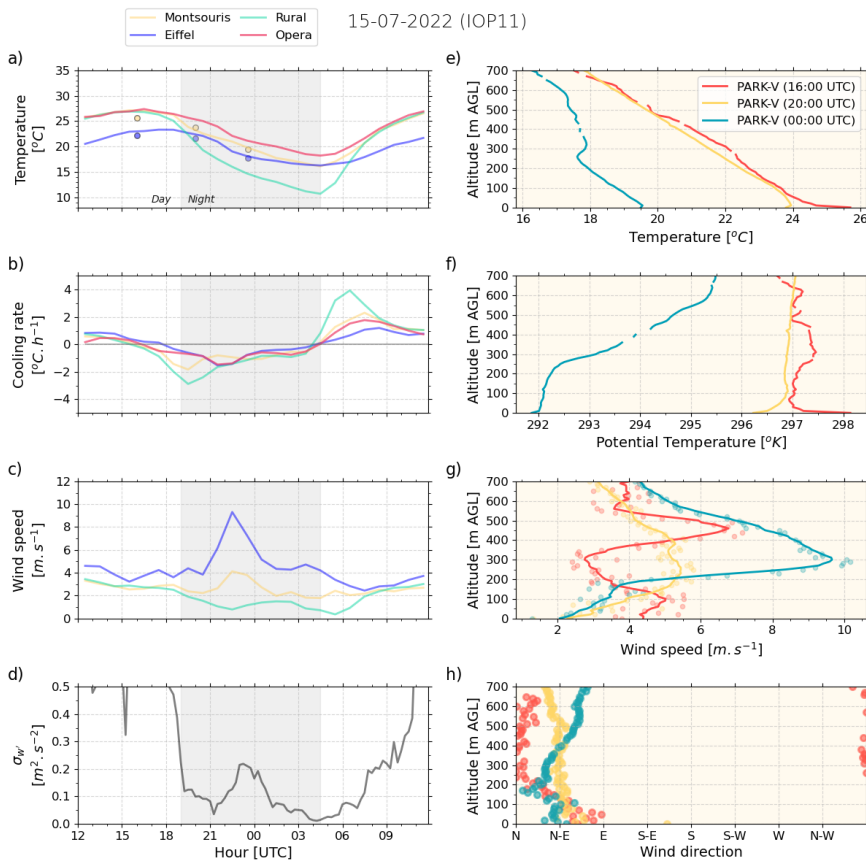
Supprimé: es

632  $s^{-1}$  near the height of the temperature inversion suggests that stably stratified air from rural  
633 surroundings is advected over the city.

634

635 The intermediary regime highlights that while the rural nocturnal layer becomes statically  
636 stable during the evening, as evidenced by the very low near-surface wind speed at the rural  
637 site, the UBL remains statically neutral. Vertical turbulent mixing in the UBL prevents a  
638 temperature inversion to form in the UCL, even above the urban green space.

639



640

641 Figure 7: same as Fig. 5 for July 15, 2022 (IOP11)

642

643

644  
645  
646  
647  
648

### 649 4.3 Turbulent regime: weak park cooling effect combined with 650 weak regional UHI intensity

651

652 The evening of 04/07, classified in the turbulent regime, is characterised by nearly identical  
653 cooling rates in built-up settings, urban green spaces, as well as aloft at the top of the Eiffel  
654 Tower. Cooling peaks near -2 to -2.5°C/hr at all locations (Fig. 8b). Wind speed at both the  
655 rural settings and the urban park does not decrease after sunset, but rather increases after  
656 18 UTC as the wind aloft picks up (Fig. 8c). In addition to the strong advection effects, the UBL  
657 remains turbulent during the night as turbulent vertical mixing remains above  $0.2 \text{ m}^2\text{s}^{-2}$  after  
658 sunset (Figure 8d), both indicating that vertical momentum transfer is not inhibited across the  
659 region.

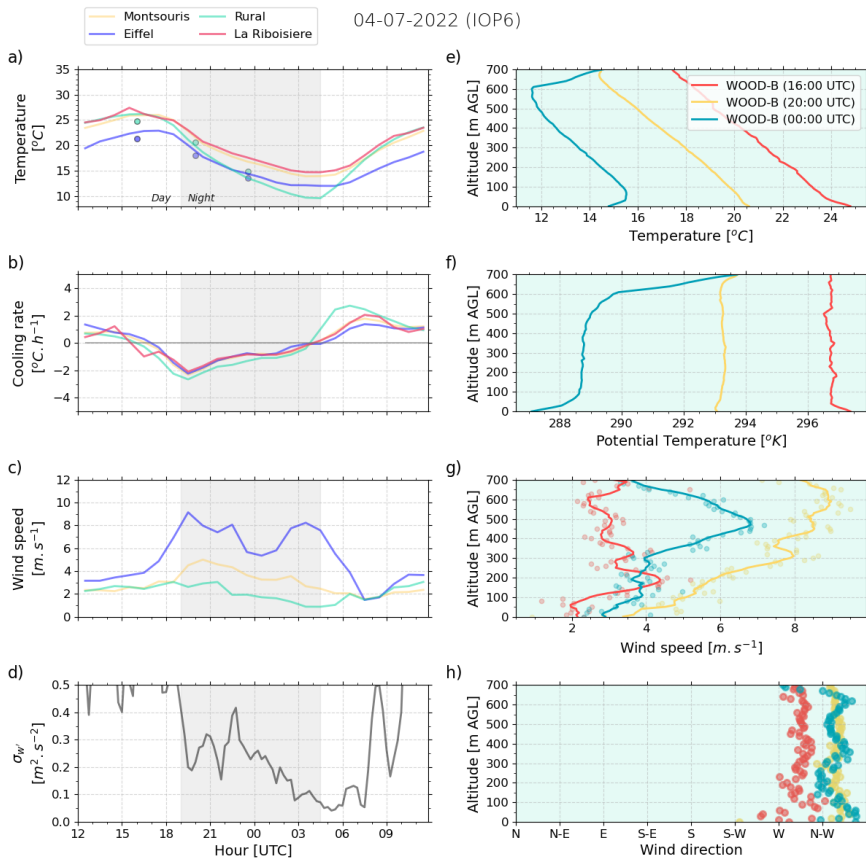
660

661 The windsound profiles carried out at the Bois de Boulogne large urban wood (WOOD-B in Fig.  
662 1), detected a neutral UBL from 0 to 700 m AGL at 20 UTC. At 00 UTC, under continued brisk  
663 turbulent mixing, a weak 1°C temperature inversion forms over the large green space while  
664 the neutral UBL extends from 100m to 600 m AGL and is capped by a 5°C temperature  
665 inversion.

666

667

668



669  
 670 Figure 8: same as Fig. 5 for July 04, 2022  
 671  
 672  
 673  
 674  
 675  
 676  
 677  
 678  
 679

## 680 5 - Characteristics and impacts of turbulence 681 regimes

682

683 To better understand the impact of wind, turbulence and static stability on differential cooling  
684 between built-up areas, urban parks and rural settings, we analyse the characteristics of the  
685 three turbulence regimes encountered during summer 2022. First, we study the diurnal  
686 evolution of wind and turbulence in built-up settings, urban green spaces and rural  
687 surroundings (Section 5.1) and then investigate the atmospheric static stability in the built-up  
688 surfaces and green infrastructures (Section 5.2) for the three regimes. Finally, we analyse the  
689 diurnal cycle of temperature and discuss the nocturnal cooling in built-up environments,  
690 green infrastructures and rural settings for the three regimes (Section 5.3).

### 691 5.1 Wind and turbulent mixing characteristics of turbulence 692 regimes

693 First, we study how wind speed evolves at diurnal scales over the city (Montsouris urban  
694 park), in the rural setting (Melun), and aloft (top of Eiffel Tower) for the turbulence regimes  
695 identified in Section 3 (Fig. 9).

696

697 In the stagnant regime (highest UHI intensity and lowest vertical velocity variance), we find  
698 that at sunset, when vertical mixing drops, the wind speed aloft increases while the near-  
699 surface wind speed decreases both over the urban park and in the rural setting (Fig. 9a).  
700 Vertical velocity variance reaches values below  $0.05 \text{ m}^2 \text{ s}^{-2}$  shortly after sunset. Not only the  
701 rural nocturnal boundary layer but also the UBL becomes stratified, thereby inhibiting vertical  
702 transfer of momentum. The stable UBL becomes decoupled from the neutral layer above,  
703 allowing near-surface wind speeds to decrease, on average below  $2 \text{ m s}^{-1}$ , through surface  
704 drag, while wind speed aloft experiences reduced friction and hence increases.

705

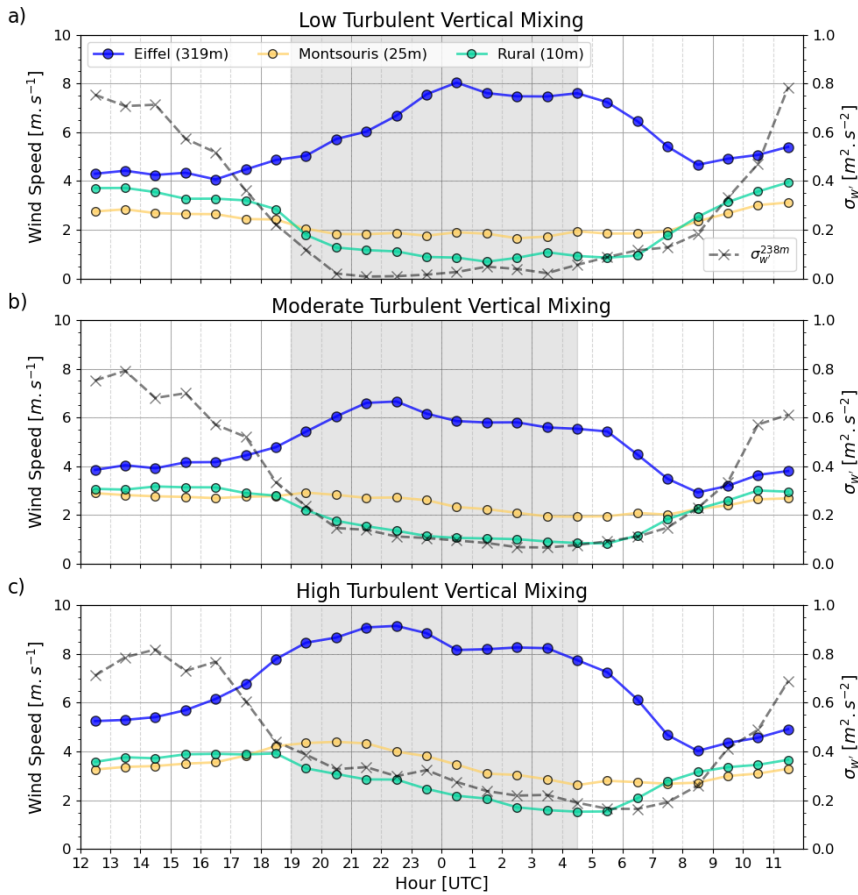
706 In the intermediate regime (strong  $\Delta\text{UHI}$  and moderate vertical velocity variance), we observe  
707 that on average, the vertical velocity variance decreases later than in the stagnant regime and  
708 it is 50 % stronger at sunset, reaching  $0.15 \text{ m}^2 \text{ s}^{-2}$  on average during the night (Fig. 9b). The

709 near-surface wind speed in the rural setting decreases at sunset similarly to the stagnant  
710 regime, so we can hypothesise that the atmosphere becomes stable in the rural environment.  
711 In the urban green spaces, the near-surface wind speed remains unchanged after sunset,  
712 which is consistent with a continued vertical transfer of momentum. Still, the stable  
713 stratification over the rural area tends to favour the formation of a low-level jet, a  
714 phenomenon that occurs in Paris in 70% of the nights in summer 2022 (Cespedes et al. 2024),  
715 so that the wind speed above the neutral UBL can double in magnitude between noon and  
716 midnight.

717

718 In the turbulent regime (low UHI intensity and high vertical velocity variance) vertical velocity  
719 variance in the UBL is on average above  $0.3 \text{ m}^2 \text{ s}^{-2}$  at sunset (Fig. 9c). Near-surface wind speed  
720 in the rural setting remains above  $3 \text{ m s}^{-1}$  on average, while central urban wind speeds  
721 increase consistently across the UBL, i.e. both near the surface and at the top of the Eiffel  
722 Tower.

723



724  
 725 Figure 9 : Average diurnal cycles over summer 2022 for each of the turbulence regimes  
 726 (stagnant at the top, intermediary in the middle, and turbulent at the bottom): wind speed  
 727 measured at Melun (rural site); Montsouris park (urban park); top of Eiffel Tower; and vertical  
 728 velocity variance at 240 m AGL derived from Doppler Lidar measurements.

Supprimé: 238

729 **5.2 Atmospheric stability characteristics of turbulence regimes**

730  
 731 In Section 4, we found evidence that the static stability above urban parks and urban woods  
 732 can vary significantly depending on the turbulent vertical mixing in the UBL. To study this  
 733 variability, we derive the potential temperature lapse rates for each windsong profile carried



735 out at 20 and 00 UTC above urban woods and parks, as well as radiosonde profiles launched  
736 at the same time from the built-up area of Bercy (URBAN-B location on Fig. 1) along the Seine  
737 river, and plot them against the vertical velocity variance estimated from the DWL  
738 measurements at the same time (Fig. 10). The potential temperature lapse rate is derived for  
739 two vertical intervals, 0-50 m AGL representing the height over which surface-based  
740 inversions are typically observed (also called park/wood internal boundary layer), and 100-  
741 200 m AGL representing the nocturnal UBL. Vertical velocity variances shown in Fig. 10 are  
742 one-hour average values. The turbulence regime derived for each evening (19-02 UTC) is also  
743 shown. Fig. 10b reveals that, when the vertical velocity variance drops below  $0.05 \text{ m}^2 \text{ s}^{-2}$   
744 (corresponding mostly to the stagnant regime) the near-surface potential temperature lapse  
745 rate above urban parks (about 20 ha) ranges  $4\text{-}6^\circ\text{C}/100 \text{ m}$  while those above the woods (about  
746 900 ha) can reach  $8\text{-}14^\circ\text{C}/100 \text{ m}$ . In the lowest vertical velocity variance conditions ( $< 0.025$   
747  $\text{m}^2 \text{ s}^{-2}$ ), near-surface potential temperature lapse rates in built-up areas also become positive  
748 ranging  $1\text{-}3^\circ\text{C}/100 \text{ m}$ . This confirms that stable stratification can occur in all settings, but the  
749 strength of the stratification depends on the surface type.

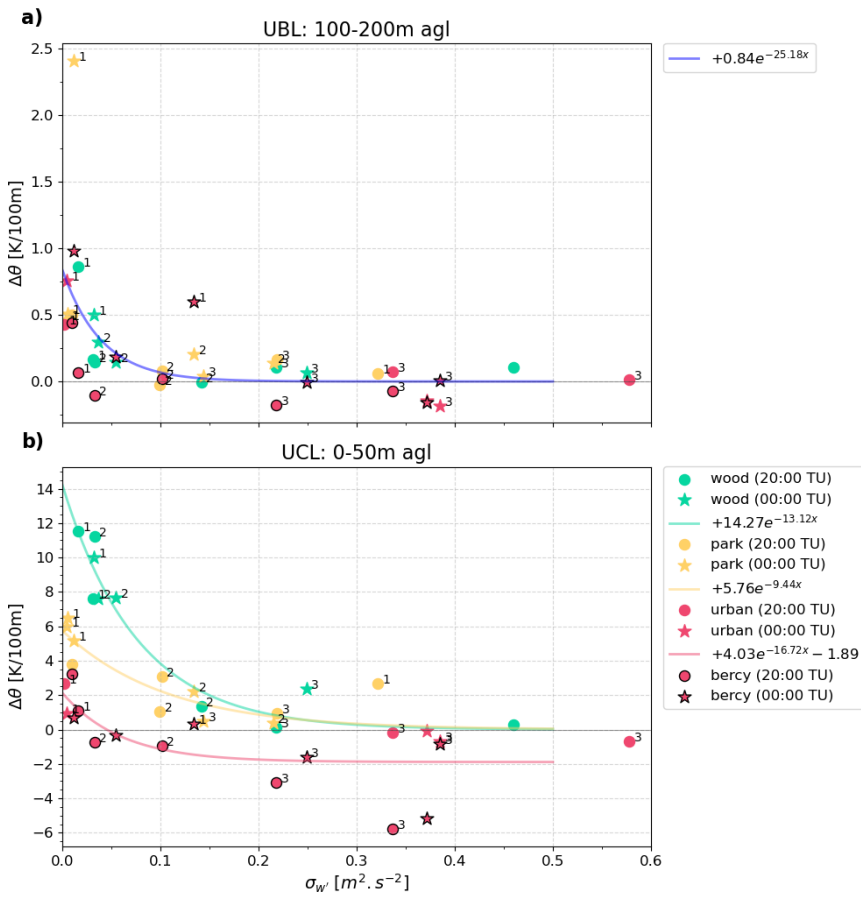
750 For vertical velocity variances ranging  $0.1\text{-}0.2 \text{ m}^2 \text{ s}^{-2}$ , near-surface potential temperature lapse  
751 rates above parks and woods range between  $0\text{-}3^\circ\text{C}/100 \text{ m}$ , decreasing to near adiabatic  
752 conditions ( $0^\circ\text{C}/100 \text{ m}$ ) as turbulent mixing increases. In built-up areas, we find that near-  
753 surface potential temperature lapse rates become negative (near  $-1^\circ\text{C}/100 \text{ m}$ ) as soon as the  
754 vertical velocity variance exceeds  $0.05 \text{ m}^2 \text{ s}^{-2}$ , a signature of a typical unstable urban surface  
755 layer.

756 This analysis provides quantitative evidence that evening and night-time air temperature  
757 conditions in the UCL become spatially heterogeneous when turbulent mixing in the UBL is  
758 very weak. Only then it is possible for a strong temperature inversion to form over the urban  
759 green space through the support of radiative flux divergence. The cool air remains in a local,  
760 internal park/wood thermal boundary layer and does not mix with the relatively warm air in  
761 the surrounding neighbourhoods. The significance and vertical extent of this cool air pool  
762 increases with green space size, and it can be speculated that also green fraction and soil  
763 moisture levels would enhance the effect.

764

765 The turbulent mixing in the UBL varies with the static stability of the UBL. As shown in Fig.  
766 10a, when the potential temperature lapse rate at 100-200 m AGL increases to values near

767 +0.5°C/100m for all settings, including built-up areas, the vertical velocity variance decreases  
 768 below 0.05 m<sup>2</sup> s<sup>-2</sup>. No clear contrast in stability is found above the different surfaces,  
 769 confirming that under the stagnant regime, the nighttime UBL is very shallow.  
 770



771

772 Figure 10: Nighttime (20 and 00 UTC) potential temperature lapse rate above wood (green),  
773 park (orange) and built-up areas (red) as a function of  $\sigma_w$  in the UBL (at 240 m AGL) for (a) a  
774 layer between 100-200 m AGL and (b) a layer between 0-50 m AGL. Symbols indicate time  
775 UTC. Urban labels with black borders correspond to data from radiosoundings launched from  
776 the URBAN-B site and the others to data from windsounds (various sites). The number shows  
777 the mean evening (19-02 UTC) turbulence regime for each case.

778

### 779 5.3 Impact of turbulence regimes on diurnal temperature 780 evolution

781

782 Ultimately, we want to determine how the turbulence regimes can impact the nocturnal  
783 cooling provided by urban green infrastructures. Figure 11 shows the mean diurnal cycles of  
784 temperature for stagnant, intermediary and turbulent regimes (a, b, and c, respectively). The  
785 temperature diurnal cycles are normalised by subtracting the temperature measured at 16  
786 UTC (peak daytime temperature). On average, daytime peak temperatures are highest for the  
787 stagnant regime near 31°C, while they peak at about 27°C for the other two regimes. Figure  
788 11 shows that after 16 UTC, the temperature at all sites decreases to a minimal value **by** the  
789 next morning at sunrise. In 12 hours, the temperatures drop between 8 and more than 14°C  
790 depending on the surface type and the turbulence regime. The stagnant regime reveals the  
791 strongest contrasts between the settings (Fig. 11a). At 00 UTC, five hours after sunset, the  
792 built-up neighbourhood cooled by 5.5°C, while the urban park cooled by 9.0°C and the rural  
793 sites by almost 13.8°C. This confirms earlier findings (Table 2 and Section 5.2) that under low  
794 turbulent vertical mixing, the radiative cooling of the surface in urban park and rural settings  
795 combined with low turbulent vertical mixing provides an efficient cooling of the near-surface  
796 atmosphere. In such conditions, urban parks can provide significantly cooler conditions than  
797 the built-up neighbourhoods nearby.

798 In the intermediary regime, the evening cooling rate in the built-up environment is slightly  
799 larger than for the stagnant regime (-6.2°C at 00 UTC, Fig. 11b). In the urban park, the  
800 increased UBL turbulent vertical mixing reduces the strength of the near-surface radiative flux  
801 divergence. The evening cooling in the urban park is not as strong (-7.5°C at 00 UTC) as in the

Supprimé: reach

803 stagnant regime. In the rural setting, the evening cooling is also reduced in the intermediary  
804 regime (-11.7°C at 00 UTC) compared to the stagnant regime, revealing that turbulence is also  
805 likely stronger in the rural nocturnal boundary layer.

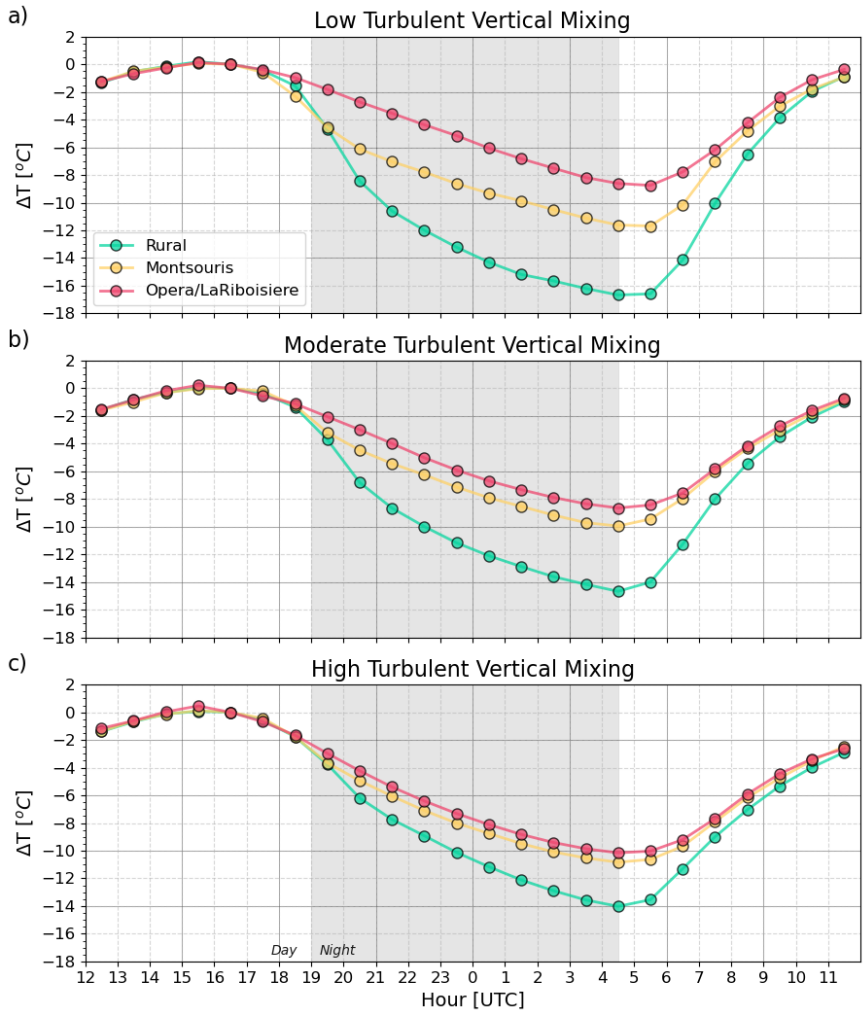
806 In the turbulent regime, with stronger turbulent vertical mixing and higher near-surface wind  
807 speed than in the other regimes, the efficiency of the surface-driven cooling in the rural  
808 setting is even more reduced, which limits the cooling compared to less turbulent conditions  
809 (-10.6°C at 00 UTC, Fig. 11c). In the built-up environment, the air temperature drops by 7.6°C  
810 between 16 and 00 UTC, i.e. 1.5-2°C more than in the other regimes. In this turbulent regime,  
811 the city centre benefits from the cooling of the rural surroundings through advection – the  
812 cooler air is mixed down into the UBL. In the urban park, two competing processes occur. The  
813 radiative flux divergence is reduced by the strong mixing, but this again means cooler air  
814 advected from rural surroundings is efficiently mixed down thereby contributing to a strong  
815 cooling also in the urban park. Hence, we find that the temperature drops by 8.3°C on average  
816 between 16 and 00 UTC, which is in between the stagnant and intermediary regime cooling.

817

818

819

820



821  
 822 Figure 11: diurnal cycle of temperature difference relative to the temperature at 16 UTC at  
 823 Melun (rural site), Montsouris park (urban park) and Opera/Lariboisiere (Built-up setting) for  
 824 stagnant, intermediary and turbulent regimes.

825

826

## 827 6) Conclusions

828 This study shows that the nocturnal cooling effect of urban parks depends on their  
829 characteristics, such as their size, but also on UBL turbulent mixing and static stability regimes  
830 that drive the relative importance of radiative and mixing transport cooling processes in the  
831 UCL. We find that turbulent vertical mixing conditions measured by a Doppler Lidar at about  
832 240 m AGL in the city centre are a very useful indicator to distinguish different evening cooling  
833 regimes in the urban environment. These findings are summarised on a schematic (Fig. 12)  
834 that represents, for each turbulent mixing regime, typical night-time vertical profiles of wind  
835 and potential temperature above the urban environment and key processes that affect  
836 nocturnal cooling.

837  
838 Highest green space nocturnal cooling intensity occurs under stable stratification in the UBL  
839 (statically stable, low turbulent mixing: vertical velocity variance of less than  $0.05 \text{ m}^2 \text{ s}^{-2}$ ) over  
840 both rural settings and urban parks. This stagnant regime is associated with large-scale  
841 subsidence and large-scale advection of warm air aloft. The potential temperature profiles  
842 above the urban parks and woods become statically stable soon after sunset due to radiative  
843 cooling of the surface and subsequent cooling of the air by radiative flux divergence, in the  
844 absence of a significant turbulent heat flux. A few hours after sunset, the entire UBL becomes  
845 on average statically stable (about 200-~~250~~ m deep) due to subsidence and advection of the  
846 stable rural air above the urban environment. Even if the heat release from the urban surface  
847 would in theory lead to an unstable/near neutral urban boundary layer at night, we observe  
848 that the strong stabilisation from above limits it strongly in height, or even totally inhibits it.  
849 At the top of the UBL, a low-level jet develops over the night with peak wind speed, but  
850 mechanical turbulence is inhibited by the static stability of the UBL. The advected rural air  
851 mass remains stable above the urban environment because of unusually low vertical mixing  
852 conditions. This stagnant regime exhibits the strongest evening cooling in both rural settings  
853 and urban parks, and the weakest cooling in the built-up environment, hence strong nocturnal  
854 temperature contrasts occur in the city depending on the vegetation fraction. In this regime,  
855 the cooling effect of green infrastructure will depend on their size and likely on the vegetation  
856 fraction of these areas. In this stagnant regime, we find comparable nocturnal cooling rates  
857 (peaking at  $-2^\circ\text{C}/\text{hr}$  around sunset) and static stability in the UCL (lapse rate near  $6^\circ\text{C}/100\text{m}$ )

Supprimé: is

Supprimé: 300

860 at 00 UTC) above the Montsouris park (15 ha) and the Eiffel tower park (24 ha) that are  
861 roughly of the same size. Above urban woods (about 900 ha) near-surface lapse rates can  
862 reach twice the value observed above urban parks (near 12°C/100m at 00 UTC). This leads to  
863 the development of an internal UBL, about 50 m (100 m) deep, above urban parks (woods).  
864

865 A second regime is identified, characterised by moderate turbulent vertical mixing in the UBL  
866 (for vertical velocity variance between 0.1 and 0.2 m<sup>2</sup>s<sup>-2</sup>). Under this intermediary regime, the  
867 potential temperature profiles above the urban park become neutral after sunset. A small  
868 temperature inversion (<1°C above urban parks, <3°C above urban woods) can be found in  
869 the UCL. A few hours after sunset, the UBL remains statically neutral up to 250-300 m due to  
870 positive turbulent heat flux at the surface and at the top of the UBL which is characterised by  
871 a temperature inversion. Advection of rural air brings a statically stable layer above the UBL.  
872 Under this intermediary regime, the evening cooling in rural settings is about 2°C less than in  
873 the stagnant regime. Two hours after sunset, the cooling in the urban park is also 2°C less  
874 than in the stagnant regime, while the built-up environment is slightly cooler than in the  
875 stagnant regime. There is probably vertical and also horizontal air mixing (advection or local  
876 turbulence), which diminishes the cooling effect of small to medium-sized parks (15-25ha) by  
877 mixing air from surrounding dense neighbourhoods. Hence, in the intermediary regime the  
878 intra-urban temperature contrasts between areas with varying vegetation fractions are  
879 significantly reduced.

880  
881 The third regime identified in this study results in the weakest nocturnal temperature  
882 contrasts. Compared to the stagnant and intermediary regimes, the turbulent regime is  
883 characterised by stronger advection and mesoscale circulation, wind shear and turbulent  
884 vertical mixing. The UBL above the urban park becomes neutral after sunset, with a depth  
885 that is significantly increased (>400 m) compared to the two other regimes. The UBL remains  
886 neutral even several hours after sunset. In this turbulent regime, the evening cooling rates  
887 are nearly identical in the built-up environment and in the urban parks. In this regime, high  
888 turbulence and wind mix the air and homogenise temperatures at a larger scale (district-to-  
889 city scale) than in the intermediary regime (neighbourhood scale), completely encompassing  
890 and erasing the cooling effect of parks.

891

Supprimé: 0.5

Supprimé: 0

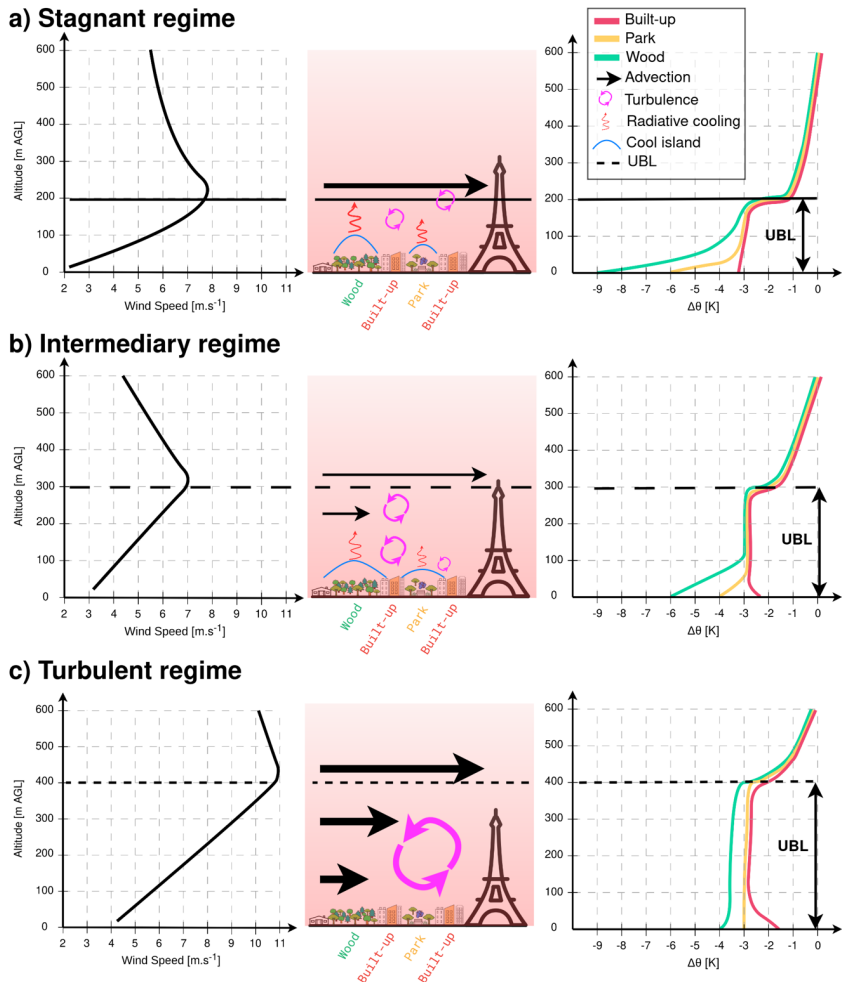
Supprimé: 6

Supprimé: the turbulent

896 As statically stable low turbulent mixing conditions occur during the strongest heat waves due  
897 to large-scale subsidence and advection of hot air, it is important to maintain spatially  
898 distributed and accessible vegetated cool island spots in the city so that people can benefit  
899 from cooler outdoor night-time conditions after being exposed to significant daytime heat  
900 stress.

901





903

904 Figure 12. Typical night-time (near 00 UTC) vertical structure of wind speed (left) and  
 905 potential temperature (right) in the urban boundary layer, observed during a)  
 906 stagnant, b) intermediate, and c) turbulent mixing regimes. Potential temperature  
 907 profiles are represented above built-up environments (red), urban parks (yellow) and  
 908 urban woods (green). Key processes (advection, turbulent mixing, radiative cooling)  
 909 affecting nocturnal cooling in the UBL are represented (centre).

Mis en forme : Police :Non Gras

910 **Data availability**

911 All raw data are available from the AERIS data centre catalogue at <https://paname.aeris->  
912 [data.fr/data-catalogue-2/](https://paname.aeris-data.fr/data-catalogue-2/).

913

914 **Author contributions**

915 MH, SK, AL, and VM planned the campaign; MH, SK, JFR, JCD and JC performed the  
916 measurements; MH, JFR, SK and JC analysed the data; MH and SK wrote the manuscript draft;  
917 JFR produced the figures; AL, VM and TN reviewed and edited the manuscript.

918

919 **Competing interests**

920 The authors declare that they have no conflict of interest.

921

922 **Acknowledgements**

923

924 The PANAME experimental program benefited from several supports, including the research  
925 project H2C funded by the French national agency for research (ANR) with the reference ANR-  
926 20-CE22-0013, the Research Demonstration Project for Paris Olympics 2024 funded by  
927 Météo-France and the Weather Meteorological Organization, the Paris Region PhD program  
928 2020, investments from DIM Q12, OBS4CLIM-PIA3, CNRS-INSU and the ACTRIS research  
929 infrastructure, and data management (AERIS national data and services center). The authors  
930 would like to thank all the volunteers and participants who contributed to the success of the  
931 SOP 2022, in particular the teams and many volunteers who carried out the windsonde  
932 releases in the parks in the evening and at night and the radiosoundings at Bercy. Thanks are  
933 extended to Hugo Ricketts for training the IPSL team to operate windsonds, with the support  
934 of the European COST action PROBE. Authors would like to express their thanks to the  
935 QUALAIR-SU scientific team who enabled the Doppler Lidar deployment on the site at

936 Sorbonne Université.

937

## 938 References

939 Aram, F. E. Higuera García, E. Solgi, S. Mansournia. Urban green space cooling effect in cities.

940 Heliyon 5 (2019) e01339. doi: [10.1016/j.heliyon.2019.e01339](https://doi.org/10.1016/j.heliyon.2019.e01339)

941 Barradas, V.L. Air temperature and humidity and human comfort index of some city parks of

942 Mexico City. *Int J Biometeorol* 35, 24–28 (1991). <https://doi.org/10.1007/BF01040959>

943

944 Rupa Basu, Jonathan M. Samet, Relation between Elevated Ambient Temperature and

945 Mortality: A Review of the Epidemiologic Evidence, *Epidemiologic Reviews*, Volume 24, Issue

946 2, December 2002, Pages 190–202, <https://doi.org/10.1093/epirev/mxf007>

947

948 Barthelmie, R. J., Grisogono, B., & Pryor, S. C. (1996). Observations and simulations of diurnal

949 cycles of near-surface wind speeds over land and sea. *Journal of Geophysical Research:*

950 *Atmospheres*, 101(D16), 21327-21337. <https://doi.org/10.1029/96JD01520>

951

952 Dahech, S., Charfi, S., & Madelin, M. (2020). Représentativité des températures mesurées

953 dans la station météorologique Paris-Montsouris. *Climatologie*, 17, 5.

954 <https://doi.org/10.1051/climat/202017005>

955

956 Bowler D. E., Lisette Buyung-Ali, Teri M. Knight, Andrew S. Pullin, Urban greening to cool

957 towns and cities: A systematic review of the empirical evidence, *Landscape and Urban*

958 *Planning*, Volume 97, Issue 3, 2010, Pages 147-155, ISSN 0169-2046,

959 <https://doi.org/10.1016/j.landurbplan.2010.05.006>

960

961 Cai, X., Yang, J., Zhang, Y. *et al.* Cooling island effect in urban parks from the perspective of

962 internal park landscape. *Humanit Soc Sci Commun* 10, 674 (2023).

963 <https://doi.org/10.1057/s41599-023-02209-5>

964

965 Chang C. C., Ming-Huang Li, Shyh-Dean Chang, A preliminary study on the local cool-island  
966 intensity of Taipei city parks, *Landscape and Urban Planning*, Volume 80, Issue 4, 2007, Pages  
967 386-395, ISSN 0169-2046, <https://doi.org/10.1016/j.landurbplan.2006.09.005>  
968

969 Céspedes, J., Kotthaus, S., Preissler, J., Toupoint, C., Thobois, L., Drouin, M.-A., Dupont, J.-C.,  
970 Fauchoux, A., and Haeffelin, M.: The Paris Low-Level Jet During PANAME 2022 and its Impact  
971 on the Summertime Urban Heat Island, *EGUsphere* [preprint],  
972 <https://doi.org/10.5194/egusphere-2024-520>, 2024.  
973

974 Doick K. J., A. Peace, T. R. Hutchings, The role of one large greenspace in mitigating London's  
975 nocturnal urban heat island, *Science of The Total Environment*, Volume 493, 2014, Pages 662-  
976 671, ISSN 0048-9697, <https://doi.org/10.1016/j.scitotenv.2014.06.048>  
977

978 Forceville G., A. Lemonsu, S. Gorla, M. Stempfelet, S. Host, J-M. Alessandrini, E. Cordeau, M.  
979 Pascal, Spatial contrasts and temporal changes in fine-scale heat exposure and vulnerability  
980 in the Paris region, *Science of The Total Environment*, Volume 906, 2024, 167476, ISSN 0048-  
981 9697, <https://doi.org/10.1016/j.scitotenv.2023.167476>  
982

983 [Gao, Z., Zaitchik, B. F., Hou, Y., & Chen, W. \(2022\). Toward park design optimization to mitigate](https://doi.org/10.1016/j.scs.2022.103870)  
984 [the urban heat Island: Assessment of the cooling effect in five US cities. \*Sustainable Cities and\*](https://doi.org/10.1016/j.scs.2022.103870)  
985 [\*Society\*, 81, 103870. https://doi.org/10.1016/j.scs.2022.103870](https://doi.org/10.1016/j.scs.2022.103870)  
986

987 Grimmond, C. S. B., and T. R. Oke, 2002: Turbulent Heat Fluxes in Urban Areas: Observations  
988 and a Local-Scale Urban Meteorological Parameterization Scheme (LUMPS). *J. Appl. Meteor.*  
989 *Climatol.*, 41, 792–810, [https://doi.org/10.1175/1520-](https://doi.org/10.1175/1520-0450(2002)041<0792:THFIUA>2.0.CO;2)  
990 [0450\(2002\)041<0792:THFIUA>2.0.CO;2](https://doi.org/10.1175/1520-0450(2002)041<0792:THFIUA>2.0.CO;2).  
991

992 Haeffelin M, Barthès L, Bock O, Boitel C, Bony S, Bouniol D, Chepfer H, Chiriaco M, Cuesta J,  
993 Delanoë J, Drobinski P, Dufresne J-L, Flamant C, Grall M, Hodzic A, Hourdin F, Lapouge F,  
994 Lemaître Y, Mathieu A, Morille Y, Naud C, Noël V, O'Hirok W, Pelon J, Pietras C, Protat A,  
995 Romand B, Scialom G, Vautard R (2005) SIRTA, a ground-based atmospheric observatory for  
996 cloud and aerosol research. *Ann Geophys* 23:253–275, <https://doi.org/10.5194/angeo-23->

997 [253-2005](#).

998

999 Holmer, B., Thorsson, S., & Lindén, J. (2013). Evening evapotranspirative cooling in relation to  
1000 vegetation and urban geometry in the city of Ouagadougou, Burkina Faso. *International*  
1001 *Journal of Climatology*, 33(15), 3089-3105 , <https://doi.org/10.1002/joc.3561>.

1002

1003 Ibsen, P. C., Borowy, D., Dell, T., Greydanus, H., Gupta, N., Hondula, D. M., ... & Jenerette, G.  
1004 D. (2021). Greater aridity increases the magnitude of urban nighttime vegetation-derived air  
1005 cooling. *Environmental Research Letters*, 16(3), 034011, DOI 10.1088/1748-9326/abdf8a

1006

1007 Keatinge W R, Donaldson G C, Cordioli E, Martinelli M, Kunst A E, Mackenbach J P et al. Heat  
1008 related mortality in warm and cold regions of Europe: observational study *BMJ* 2000; 321 :670  
1009 doi:10.1136/bmj.321.7262.670

1010

1011 Laj, P., Lund Myhre, C., Riffault, V., Amiridis, V., Fuchs, H., Eleftheriadis, K., ... & Vana, M.  
1012 (2024). Aerosol, Clouds and Trace Gases Research Infrastructure—ACTRIS, the European  
1013 research infrastructure supporting atmospheric science. *Bulletin of the American*  
1014 *Meteorological Society*. <https://doi.org/10.1175/BAMS-D-23-0064.1>

1015

1016 Lemonsu, A., Belair, S. & Mailhot, J. The New Canadian Urban Modelling System: Evaluation  
1017 for Two Cases from the Joint Urban 2003 Oklahoma City Experiment. *Boundary-Layer*  
1018 *Meteorol* 133, 47–70 (2009). <https://doi.org/10.1007/s10546-009-9414-2>

1019

1020 Lemonsu, A., V. Vigiúí, M. Daniel, V. Masson, Vulnerability to heat waves: Impact of urban  
1021 expansion scenarios on urban heat island and heat stress in Paris (France), *Urban Climate*,  
1022 Volume 14, Part 4, 2015, Pages 586-605, ISSN 2212-0955,  
1023 <https://doi.org/10.1016/j.uclim.2015.10.007>.

1024

1025 Lemonsu, A., J.M. Alessandrini, J. Capo, M. Claeys, E. Cordeau, C. de Munck, S. Dahech, J.C.  
1026 Dupont, F. Dugay, V. Dupuis, G. Forceville, S. Garrigou, O. Garrouste, M. Goret, S. Gorla, M.  
1027 Haeffelin, S. Host, C. Joly, P. Keravec, S. Kotthaus, N. Laruelle, M. Madelin, V. Masson, C.  
1028 Mauclair, T. Nagel, M. Pascal, J.F. Ribaud, G. Roberts, A. Rosso, A. Roy, M. Sabre, O. Sanchez,

1029 M. Stempfelet, W. Wei, R. Wilson, J. Wurtz, The heat and health in cities (H2C) project to  
1030 support the prevention of extreme heat in cities, *Climate Services*, 2024, 100472, ISSN 2405-  
1031 8807, <https://doi.org/10.1016/j.cliser.2024.100472>  
1032  
1033 Lemonsu A., Barrau S., Capo J., Céspedes J., Dahech S., de Munck C., Dumas G., Dupont J.-C.,  
1034 Dupuis V., Etienne J.-C., Garrouste O., Goret M., Haeffelin M., Keravec P., Kotthaus S., Madelin  
1035 M., Martinet P., Masson V., Nagel T., Price J., Ribaud J.-F., Rivollet M., Roberts G., Roy A.,  
1036 Unger, V., Wilson R., Wallois S., Wurtz J., Multi-scale study of urban-atmosphere interactions  
1037 in the Paris region (France) in the framework of the PANAME experiment, *Bull. Am. Met. Soc.*  
1038 Submitted 2024.  
1039  
1040 Lin, Y., C. Wang, J. Yan, J. Li, and S. He, 2022: Observation and Simulation of Low-Level Jet  
1041 Impacts on 3D Urban Heat Islands in Beijing: A Case Study. *J. Atmos. Sci.*, 79, 2059–2073,  
1042 <https://doi.org/10.1175/JAS-D-21-0245.1>.  
1043  
1044 Martilli, A., 2002: Numerical Study of Urban Impact on Boundary Layer Structure: Sensitivity  
1045 to Wind Speed, Urban Morphology, and Rural Soil Moisture. *J. Appl. Meteor. Climatol.*, 41,  
1046 1247–1266, [https://doi.org/10.1175/1520-0450\(2002\)041<1247:NSOUIO>2.0.CO;2](https://doi.org/10.1175/1520-0450(2002)041<1247:NSOUIO>2.0.CO;2).  
1047  
1048 Morris, C. J. G., I. Simmonds, and N. Plummer, 2001: Quantification of the Influences of Wind  
1049 and Cloud on the Nocturnal Urban Heat Island of a Large City. *J. Appl. Meteor. Climatol.*, 40,  
1050 169–182, [https://doi.org/10.1175/1520-0450\(2001\)040<0169:QOTIOW>2.0.CO;2](https://doi.org/10.1175/1520-0450(2001)040<0169:QOTIOW>2.0.CO;2).  
1051  
1052 Murage, Peninah; Hajat, Shakoore; Kovats, R. Sari. Effect of night-time temperatures on cause  
1053 and age-specific mortality in London. *Environmental Epidemiology* 1(2):p e005, December  
1054 2017. | DOI: 10.1097/EE9.0000000000000005  
1055  
1056 Oke, T. R. (1976). The distinction between canopy and boundary-layer urban heat islands.  
1057 *Atmosphere*, 14(4), 268–277. <https://doi.org/10.1080/00046973.1976.9648422>  
1058

1059 Oke, T.R. (1982), The energetic basis of the urban heat island. Q.J.R. Meteorol. Soc., 108: 1-  
1060 24. <https://doi.org/10.1002/qj.49710845502>  
1061  
1062 Oke, T. Towards better scientific communication in urban climate. *Theor. Appl. Climatol.* 84,  
1063 179–190 (2006). <https://doi.org/10.1007/s00704-005-0153-0>  
1064  
1065 Oke, T. R., Mills, G., Christen, A., & Voogt, J. A. (2017). *Urban climates*. Cambridge University  
1066 Press.  
1067  
1068 Pirard P, Vandentorren S, Pascal M, Laaidi K, Le Tertre A, Cassadou S, Ledrans M. Summary of  
1069 the mortality impact assessment of the 2003 heat wave in France. *Euro Surveill.*  
1070 2005;10(7):pii=554. <https://doi.org/10.2807/esm.10.07.00554-en>  
1071  
1072 von Rohden, C., Sommer, M., Naebert, T., Motuz, V., & Dirksen, R. J. (2022). Laboratory  
1073 characterisation of the radiation temperature error of radiosondes and its application to the  
1074 GRUAN data processing for the Vaisala RS41. *Atmospheric Measurement Techniques*, 15(2),  
1075 383-405.  
1076  
1077 Royé, Dominic; Sera, Francesco; Tobías, Aurelio; Lowe, Rachel; Gasparrini, Antonio; Pascal,  
1078 Mathilde; de'Donato, Francesca; Nunes, Baltazar; Teixeira, Joao Paulo. Effects of Hot Nights  
1079 on Mortality in Southern Europe. *Epidemiology* 32(4):p 487-498, July 2021. | DOI:  
1080 10.1097/EDE.0000000000001359  
1081  
1082 Shashua-Bar, L., M.E. Hoffman, Vegetation as a climatic component in the design of an urban  
1083 street: An empirical model for predicting the cooling effect of urban green areas with trees,  
1084 *Energy and Buildings*, Volume 31, Issue 3, 2000, Pages 221-235, ISSN 0378-7788,  
1085 [https://doi.org/10.1016/S0378-7788\(99\)00018-3](https://doi.org/10.1016/S0378-7788(99)00018-3)  
1086  
1087 Steeneveld, G. J., B. J. H. van de Wiel, and A. A. M. Holtslag, 2006: Modeling the Evolution of  
1088 the Atmospheric Boundary Layer Coupled to the Land Surface for Three Contrasting Nights in  
1089 CASES-99. *J. Atmos. Sci.*, 63, 920–935, <https://doi.org/10.1175/JAS3654.1>.  
1090

1091 Steeneveld, G. J., M. J. J. Wokke, C. D. Groot Zwaaftink, S. Pijlman, B. G. Heusinkveld, A. F. G.  
1092 Jacobs, and A. A. M. Holtslag (2010), Observations of the radiation divergence in the surface  
1093 layer and its implication for its parameterization in numerical weather prediction models, *J.*  
1094 *Geophys. Res.*, 115, D06107, doi:[10.1029/2009JD013074](https://doi.org/10.1029/2009JD013074).  
1095  
1096 Taha, H., Akbari, H. & Rosenfeld, A. Heat island and oasis effects of vegetative canopies:  
1097 Micro-meteorological field-measurements. *Theor Appl Climatol* 44, 123–138 (1991).  
1098 <https://doi.org/10.1007/BF00867999>  
1099  
1100 Tsiringakis, A., Theeuwes, N.E., Barlow, J.F. *et al.* Interactions Between the Nocturnal Low-  
1101 Level Jets and the Urban Boundary Layer: A Case Study over London. *Boundary-Layer*  
1102 *Meteorol* **183**, 249–272 (2022). <https://doi.org/10.1007/s10546-021-00681-7>  
1103  
1104 Zhu, W.; Sun, J.; Yang, C.; Liu, M.; Xu, X.; Ji, C. How to Measure the Urban Park Cooling Island?  
1105 A Perspective of Absolute and Relative Indicators Using Remote Sensing and Buffer Analysis.  
1106 *Remote Sens.* 2021, 13, 3154. <https://doi.org/10.3390/rs13163154>  
1107  
1108  
1109  
1110  
1111

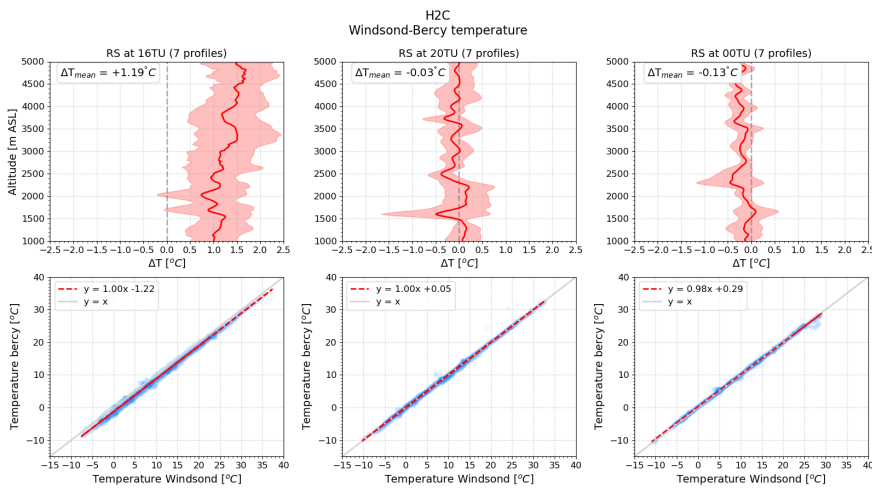


1112 **Appendix A: Windsond temperature profiles**  
1113 **assessment**

1114

1115 The evaluation of the Windsond temperature profiles was conducted by comparing them with  
1116 the Vaisala RS41 temperature profiles launched at Quai de Bercy (URBAN-B site in Fig. 1)  
1117 during the SOP 2022. Data from seven IOPs were used for this evaluation, with profiles  
1118 recorded at 16:00, 20:00, and 00:00 UTC, respectively. Von Rohden et al (2022) find a  
1119 radiation bias of 0.1°C in Vaisala RS41 temperature data in the troposphere. Our comparisons  
1120 reveal an average warm bias of 1.2°C in windsond temperature profiles compared to Vaisala  
1121 RS41 values of 16 UTC profiles. No significant bias is found at 20 and 00 UTC.

1122



1123

1124 Figure A1: Assessment of windsond temperature profiles. a-c) Average temperature  
1125 differences between the Windsond and Vaisala RS-41 temperature profiles from 1000m to  
1126 5000m ASL at 16, 20 and 00 UTC respectively. d-f) Point-to-point correlations between  
1127 Windsond and Vaisala RS-41 temperatures.

1128

1129

1130